

# JGR Planets

## RESEARCH ARTICLE

10.1029/2021JE006825

### Key Points:

- A H<sub>2</sub>-CO<sub>2</sub> greenhouse can warm early Mars above the freezing point of water
- Low obliquity is more conducive to rainfall over locations with valley network formations
- Fully coupled dynamic oceans in the northern hemisphere or Hellas basin do not significantly alter the ancient climate

### Supporting Information:

Supporting Information may be found in the online version of this article.

### Correspondence to:

S. D. Guzewich,  
[scott.d.guzewich@nasa.gov](mailto:scott.d.guzewich@nasa.gov)








### Citation:

Guzewich, S. D., Way, M. J., Aleinov, I., Wolf, E. T., Del Genio, A., Wordsworth, R., & Tsigaridis, K. (2021). 3D simulations of the early martian hydrological cycle mediated by a H<sub>2</sub>-CO<sub>2</sub> greenhouse. *Journal of Geophysical Research: Planets*, 126, e2021JE006825. <https://doi.org/10.1029/2021JE006825>

Received 8 JAN 2021  
 Accepted 17 JUN 2021

© 2021. American Geophysical Union.  
 All Rights Reserved.

# 3D Simulations of the Early Martian Hydrological Cycle Mediated by a H<sub>2</sub>-CO<sub>2</sub> Greenhouse

Scott D. Guzewich<sup>1,3</sup> , Michael J. Way<sup>2,3,4</sup> , Igor Aleinov<sup>2,3,5</sup> , Eric T. Wolf<sup>3,6,7</sup> , Anthony Del Genio<sup>2,3</sup> , Robin Wordsworth<sup>8</sup> , and Kostas Tsigaridis<sup>2,3,5</sup> 

<sup>1</sup>NASA Goddard Space Flight Center, Greenbelt, MD, USA, <sup>2</sup>NASA Goddard Institute for Space Studies, New York, NY, USA, <sup>3</sup>NASA GSFC Sellers Exoplanet Environments Collaboration, Greenbelt, MD, USA, <sup>4</sup>Theoretical Astrophysics, Department of Physics and Astronomy, Uppsala University, Uppsala, Sweden, <sup>5</sup>Columbia University, New York, NY, USA, <sup>6</sup>University of Colorado Boulder, Boulder, CO, USA, <sup>7</sup>NASA Nexus for Exoplanet System Science, Virtual Planetary Laboratory Team, University of Washington, Seattle, WA, USA, <sup>8</sup>Department of Earth and Planetary Science, Harvard University, Cambridge, MA, USA

**Abstract** For decades, the scientific community has been trying to reconcile abundant evidence for fluvial activity on Noachian and early Hesperian Mars with the faint young Sun and reasonable constraints on ancient atmospheric pressure and composition. Recently, the investigation of H<sub>2</sub>-CO<sub>2</sub> collision-induced absorption has opened up a new avenue to warm Noachian Mars. We use the ROCKE-3D global climate model to simulate plausible states of the ancient Martian climate with this absorptive warming and reasonable constraints on surface paleopressure. We find that 1.5–2 bar CO<sub>2</sub>-dominated atmospheres with ≥3% H<sub>2</sub> can produce global mean surface temperatures above freezing, while also providing sufficient warming to avoid surface atmospheric CO<sub>2</sub> condensation at 0°–45° obliquity. Simulations conducted with both modern topography and a paleotopography, before Tharsis formed, highlight the importance of Tharsis as a cold trap for water on the planet. Additionally, we find that low obliquity (modern and 0°) is more conducive to rainfall over valley network locations than high (45°) obliquity.

**Plain Language Summary** Much evidence tells us that ancient Mars had liquid water on its surface. But reconciling that with the fainter young Sun and reasonable constraints on Mars' early atmosphere is challenging. We use a 3D global climate model with an atmosphere containing some amount of hydrogen (a possible greenhouse gas) to study Mars' early hydrological cycle and compare it to the geological evidence of surface liquid water billions of years ago. We find that hydrogen and carbon dioxide together in an atmosphere twice as thick as modern Earth can warm early Mars above the freezing point of water and that a low axial tilt produces rainfall patterns that best match the geologic evidence.

## 1. Introduction

Abundant geologic evidence strongly implies that surface liquid water was widespread on ancient Mars approximately 3.5–4 billion years ago, in the time period termed the Noachian. Such evidence includes riverine channels (e.g., Hynek et al., 2010; Hynek & Phillips, 2001; Masursky, 1973; Pieri, 1980), craters filled with sedimentary deposits and including inflow and outflow channels (e.g., Fassett & Head, 2005; Irwin et al., 2005; Schon et al., 2012), minerals that only form in the presence of liquid water (e.g., Carter et al., 2013; Ehlmann et al., 2011; Murchie et al., 2009), and features implying aqueous erosion (e.g., Carr, 1996; Malin & Edgett, 2000).

Work to deduce what climatic conditions were possible to produce such geologic evidence has been ongoing for decades, and Wordsworth (2016) provides a recent review of the state of knowledge. One-dimensional radiative-convective models were initially used (e.g., Pollack, 1979; Pollack et al., 1987) and habitable conditions (typically defined as global mean surface temperatures above 0°C) were generated with sufficiently large surface air pressures of CO<sub>2</sub>-dominated atmospheres, even with the ~25% dimmer young Sun, although not in all models (e.g., Postawko & Kuhn, 1986). Kasting (1991) showed that CO<sub>2</sub>-H<sub>2</sub>O atmospheres alone were insufficient to warm ancient Mars due to increased Rayleigh scattering at high pressure and CO<sub>2</sub> ice condensation on the surface. Increasing sophistication of the models (e.g., incorporation of cloud

effects) over time and doubts about the plausibility of very thick (>2 bar) atmospheres made reconciling the geologic evidence challenging. A plethora of greenhouse mixtures (CH<sub>4</sub>, NH<sub>3</sub>, SO<sub>2</sub>, cirrus clouds, and others) have been proposed, but all have unique problems being retained in a putative ancient atmosphere (e.g., Kasting, 1997; Kerber et al., 2015; Kuhn & Atreya, 1979; Mischna et al., 2013; Tian et al., 2010; Turbet, Gillmann, et al., 2020; Urata & Toon, 2013). More recently, indirect evidence (e.g., crater counting statistics) has implied that the ancient martian atmospheric pressure was likely less than 1 bar, with perhaps 2 bar being consistent with the data, at least for geologically short time periods (Cassata et al., 2012; Kite et al., 2014; Manga et al., 2012; Warren et al., 2019).

Limiting ancient martian atmospheric pressure to terrestrial-comparable levels in combination with the Faint Young Sun presents a strong challenge to long-term (i.e., tens to hundreds of millions of years) “warm and wet” conditions. More punctuated and brief warm climate periods interspersed with cold and dry conditions (perhaps with seasonal melting) also may fit some of the geologic evidence while also being consistent with Mars general circulation models (Cassanelli & Head, 2015; Fastook et al., 2012; Fastook & Head, 2015; Wordsworth et al., 2013, 2015). Yet, some geologic evidence (e.g., Grant et al., 2014; Grotzinger et al., 2014; Kite et al., 2017; Williams et al., 2013) still requires some persistent duration of warm and wet conditions. Recently, H<sub>2</sub> has been offered as another possible greenhouse gas (Ramirez et al., 2014; Wordsworth & Pierrehumbert, 2013). Importantly, collision-induced absorption (CIA) between H<sub>2</sub> and CO<sub>2</sub> has been shown to be efficacious at generating considerable warming through *ab initio* calculations (Wordsworth et al., 2017) and experiments (Godin et al., 2020; Mondelain et al., 2021; Turbet, Boulet, & Karman, 2020; Turbet & Forget, 2019), although the experimental results demonstrate slightly more modest absorption than the *ab initio* calculations.

One-dimensional climate models including CIA between H<sub>2</sub>, CO<sub>2</sub>, and CH<sub>4</sub> generate global mean surface temperatures above the freezing point of water for reasonable atmospheric pressures during the Noachian period (Batalha et al., 2015; Hayworth et al., 2020; Ramirez et al., 2014; Wordsworth et al., 2017). Three-dimensional general circulation models (GCMs) have also begun experiments including such CIA absorption (Kamada et al., 2020). One challenge that remains, however, is retaining comparatively large partial pressures of H<sub>2</sub>, which should have escaped rapidly during a time period when the Sun was more active (e.g., Jakosky et al., 2018). Ramirez et al. (2014) suggested the martian mantle may be more reduced and thus emit more H<sub>2</sub> relative to Earth, while still producing CO<sub>2</sub> through chemical processes in the atmosphere (see Hirschmann & Withers (2008), which implies reduced CO<sub>2</sub> outgassing from a reduced mantle). Water-rock chemical reactions (particularly with iron-bearing materials) could have generated substantial H<sub>2</sub> fluxes (Hurowitz et al., 2010; Tarnas et al., 2018; Tosca et al., 2018). Haberle et al. (2019) suggests that iron-rich meteorites impacting Mars would have degassed abundant H<sub>2</sub>, creating large H<sub>2</sub> partial pressures for short durations (up to 10<sup>4</sup> years for 100-km-sized objects) following the impact.

In this work, we examine two science questions related to the early martian climate:

1. What range of atmospheric pressure and greenhouse gas mixtures can permit global mean annual surface temperatures above the freezing point of water?
2. What is the fate of liquid water on the surface of ancient Mars?

We have performed a range of GCM simulations with the Resolving Orbital and Climate Keys of Earth and Extraterrestrial Environments with Dynamics 1.0 (ROCKE-3D) general circulation model to study these questions. Our radiative transfer model employs the CIA absorption as described by Wordsworth et al. (2017), and is flexible enough to allow varying surface pressures, gas mixtures, and global water inventories. In Section 2 we describe our methodologies and the radiative transfer scheme in detail. In Section 3 we present and discuss our results. Finally, in Section 4 we conclude.

## 2. Methodology

We employ the ROCKE-3D GCM for our simulations. Way et al. (2017) describes the physics parameterizations and broad capabilities of ROCKE-3D to simulate rocky planet atmospheres both in and out of the Solar System. Within the Solar System, ROCKE-3D has been used to study possible paleo-environments of early Venus (Way & Del Genio, 2020; Way et al., 2016, 2018) and transient atmospheres on Earth's Moon

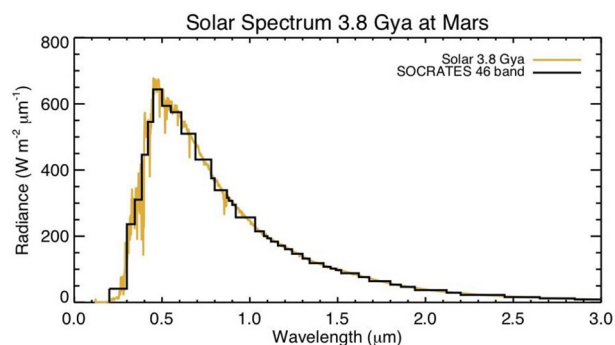


**Figure 1.** The stellar spectrum at 3.8 Ga (orange) along with the 46-band discretization of this stellar spectrum used in our SOCRATES shortwave radiative transfer calculation (black).

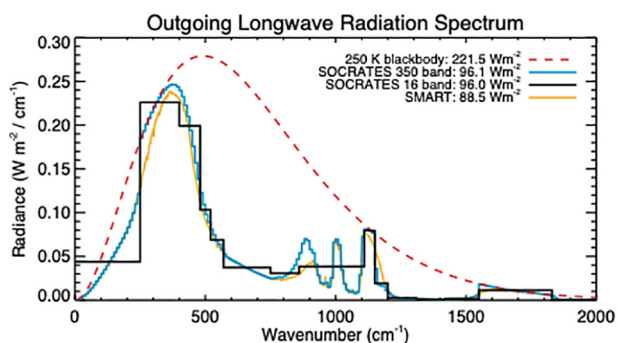


**Figure 2.** Outgoing longwave radiation spectrum from a 250 K blackbody (red dashed) and from 1-D offline radiative transfer calculations using SOCRATES at high resolution (blue), the general circulation model (GCM) resolution (black), and SMART (orange). Here we have assumed a 2-bar CO<sub>2</sub>-only atmosphere with a 250 K surface temperature and 167 K isothermal stratosphere. Our model underestimates absorption by a pure CO<sub>2</sub> atmosphere. Note, that here we have used the ab initio CO<sub>2</sub>-H<sub>2</sub> and CO<sub>2</sub>-CH<sub>4</sub> collision-induced absorption (CIA) from Wordsworth et al. (2017). However, recent laboratory work by Turbet, Boulet, and Karman (2020) argues that the Wordsworth CIAs overestimate their greenhouse effect. Further note that Godin et al. (2020) independently conducted laboratory measurements of CO<sub>2</sub>-H<sub>2</sub> and CO<sub>2</sub>-CH<sub>4</sub> CIAs which are in agreement with those measured by Turbet, Boulet, and Karman (2020). To test potential biases, here we have performed off-line calculations with SOCRATES to assess the differences between the Wordsworth et al. (2017) and Turbet, Boulet, and Karman (2020) CIAs. For a 2-bar atmosphere with 99% CO<sub>2</sub> and 1% CH<sub>4</sub>, the Wordsworth et al. (2017) CIA reduce the outgoing longwave radiation (OLR) by ~4 Wm<sup>-2</sup> compared to the Turbet, Boulet, and Karman (2020) CIA. Likewise, for an atmosphere with 95% CO<sub>2</sub> and 5% H<sub>2</sub>, the Wordsworth et al. (2017) CIA reduce the OLR by ~8 Wm<sup>-2</sup> compared to the Turbet, Boulet, and Karman (2020) CIA. See the supporting information Figures S5–S8 for comparisons of longwave fluxes and radiative cooling rates between the two CIA formulations along with an expanded discussion.

(Aleinov et al., 2019). ROCKE-3D is freely available for download at <https://simplex.giss.nasa.gov/gcm/ROCKE-3D/>, and instructions for set-up and testing are provided.

ROCKE-3D has heritage from the NASA Goddard Institute for Space Studies ModelE2 and employs many facets of that terrestrial climate model, including the dynamical core and many physical parameterizations (e.g., water ice cloud physics, fractional stratiform cloud cover and cumulus parameterizations, surface and subsurface runoff, ocean dynamics, etc.). As a GCM designed to simulate hypothetical exoplanet environments and ancient conditions in our Solar System, several modifications were required in the transition from ModelE2 to ROCKE-3D. First among these is the adoption of the Suite of Community Radiative Transfer codes (SOCRATES) radiation scheme (e.g., Amundsen et al., 2016) that is adaptable to non-terrestrial gas mixtures, varying stellar insolation, and stellar type. SOCRATES uses a two-stream radiative transfer solver with correlated-k distributions to solve for shortwave and longwave absorption and scattering (Edwards, 1996; Edwards & Slingo, 1996). SOCRATES can be flexibly configured to suit particular atmospheric gas mixtures, stellar spectra, and spectral resolutions. Here, SOCRATES has been configured specifically for paleo Mars atmospheres, suitable for multi-bar CO<sub>2</sub> dominated atmospheres, along with H<sub>2</sub>O, CH<sub>4</sub>, H<sub>2</sub>, and N<sub>2</sub> at lesser amounts. Gas absorption is included via the current best practices. CO<sub>2</sub> line absorption is included with a sub-Lorentzian line shape truncated at 500 cm<sup>-1</sup> from the line centers. H<sub>2</sub>O and CH<sub>4</sub> line absorption assumes a Voigt profile truncated at 25 cm<sup>-1</sup> from the line centers. The H<sub>2</sub>O self- and foreign-broadened continua are included using the MT\_CKD version 3.0 continuum model (Clough et al., 2005), and collision induced absorption (CIA) for CO<sub>2</sub>-CO<sub>2</sub> and other important pairs are also included.

Figure 1 shows the input stellar spectrum used in this work, taken as the Sun spectrum at 3.8 Ga from Claire et al. (2012) with the spectral scaling calibrated to Lean et al. (1995), and with the total solar flux scaled to Mars at this time period (442 Wm<sup>-2</sup>). Our Sun has slowly brightened over time (Gough, 1981), and at 3.8 Ga the Sun was only ~75% as luminous as it is today. Also, at this time period, the Sun was slightly redder, with an effective temperature about ~100 K cooler than it is today (Claire et al., 2012). The result of the effective temperature change is that slightly more radiation is emitted in the near-infrared compared to the visible, relative to the present-day Sun. In practice, assuming an identical incident stellar flux, the downwelling stellar flux that reaches the surface through a nominal early Mars-like atmosphere is lessened by only a few tenths of a Wm<sup>-2</sup> compared to the using the present-day Sun spectrum. Overlaid on Figure 1 are the 46 shortwave bands used in our model. Previous works have shown that adequate shortwave radiative transfer performance requires resolving absorption bands and windows in the near-infrared (Yang et al., 2016). Thus, 46 bands were used to parse out H<sub>2</sub>O, CO<sub>2</sub>, and CH<sub>4</sub> absorption in this spectral region.

The longwave bands also account for CO<sub>2</sub>, H<sub>2</sub>O, CH<sub>4</sub>, and the CIA coefficients. Figure 2 illustrates an example of the longwave performance of our radiative transfer model restricted to CO<sub>2</sub>. Here, duplicating previously published calculations, we assume a 2-bar pure CO<sub>2</sub> atmosphere with a 250 K surface temperature, a dry adiabatic lapse rate, and a 167 K isothermal stratosphere. We compare radiative transfer calculations from SOCRATES using the GCM resolution (16 bands), a high-resolution

configuration of SOCRATES (350 bands), and also with published calculations using SMART (see Kopparapu et al., 2013, Figure 1). Our SOCRATES calculations, both with the GCM resolution and high-resolution versions, underestimate CO<sub>2</sub> absorption thus allowing more outgoing longwave radiation (OLR) by  $\sim 7.5 \text{ Wm}^{-2}$  compared with SMART calculations at  $88.5 \text{ Wm}^{-2}$ . Identical calculations conducted by Wordsworth et al. (2010) using a two-stream correlated-k approach indicate an OLR of  $88.17 \text{ Wm}^{-2}$ . However, more recent calculations featured in Wordsworth et al. (2017, Supporting information), that used a line-by-line multi-stream approach, yielded an OLR of  $\sim 92 \text{ Wm}^{-2}$ , a step closer toward our SOCRATES results. By either comparison, our model features somewhat weaker thermal absorption by CO<sub>2</sub> compared with other published results, meaning that our pure-CO<sub>2</sub> simulations may yield slightly colder surface temperatures than other codes. See the supporting information Figures S1–S4 for comparisons of shortwave and longwave fluxes and radiative heating/cooling rates between SOCRATES and SMART for pure CO<sub>2</sub> atmospheres along with an expanded discussion.

The surface hydrological cycle is represented by a system of dynamic lakes and a groundwater scheme. The lakes are assumed to have a conical shape, so they change their exposed area depending on the amount of stored water. If the amount of stored water exceeds a pre-defined sill depth, the excess of water is moved to the lake system in a neighboring cell according to a prescribed river routing scheme. If no river routing is prescribed for a particular cell, the lake is allowed to grow there indefinitely. The ground hydrology part employs a six-layer soil scheme (Abramopoulos et al., 1988; Rosenzweig & Abramopoulos, 1997) with the upper layer being 0.1 m deep and the rest growing geometrically with depth up to a total of 3.5 m. The thermal and hydrological properties of each layer are computed according to the prescribed composition of soil components (sand, clay, silt) and present water. The heat between the layers is exchanged according to the thermal conductivity law and can be transported by water. The water can drain to the lower layers due to gravity (according to Darcy's law) or it can be taken to the upper layers by capillary uplifting. The amount of water in each layer is not allowed to exceed the saturation level or fall below the hygroscopic minimum, which are defined by the local soil texture. The bottom of the lowest layer is assumed to be impermeable to heat and water. Part of the water from each layer can be lost to underground runoff, which is assumed to be proportional to the local slope. The local slope is typically prescribed according to the local topography at scales of 10–1,000 m. Since for the Noachian period we do not know the topography at that resolution (which may not necessarily correlate with the global topography), for the local slope we used a typical value for a flat modern Earth desert uniformly over the planet. The upper soil layer can also experience surface runoff, which depends on its level of saturation and the strength of the rainstorm. All runoff water is redirected to the local lakes. All heat and water exchange with the atmosphere is performed through the upper layer. The upper layer of soil receives water from precipitation and condensation and loses it through evaporation and runoff. If the precipitation is in a solid form, the ground hydrology algorithm forms a snowpack. The snowpack is represented by a three-layer snow model with its own melting and refreezing cycle. The fraction of the ground covered by snow is defined by the snow thickness and local topography. The lakes can also form lake ice when the amount of heat in the lake falls below the freezing threshold, and they can accumulate snow on top of the ice. The albedo of the surface is defined as a weighted average of the albedos of bare soil, open water, and sea/lake ice and snow, according to their fractions. The albedo of bare soil is prescribed for dry soil as discussed below, but can decrease when the soil gets wet. The albedos of open water, sea/lake ice and snow use modern Earth parametrization (see Hansen et al., 1983; Schmidt et al., 2006, and references therein). In particular, the albedo of the snow depends on the grain size and is assumed to decrease with age (Hansen et al., 1983).

For our ancient Mars simulations discussed in this work, we run the model at 4° latitude by 5° longitude resolution with 40 vertical atmospheric layers from the surface (500–2,000 mb) to  $\sim 0.1$  mb at the top. Mars orbital parameters use modern values except for specific simulations where obliquity is changed as discussed below. Similarly, we use modern Mars topography for simplicity in most simulations and initialize the surface as having uniform 15% broadband albedo with sandy soil. It's reasonable to assume that the Noachian surface could have been darker than the modern due to less surface oxidation, although snow and ice cover could have offset that to some degree. Of course, the true Noachian surface albedo is unknown, but note this value of 15% is lower than some other Noachian Mars climate simulations, many of which use modern surface albedo distributions (e.g., Forget et al., 2013; Mischna et al., 2013), although Mischna et al. (2013) also experimented with lower (8%–12%) northern hemisphere albedo to mimic plausible unoxidized fresh

**Table 1**  
ROCKE-3D Simulations

Simulation	Surface pressure (bar)	% CO <sub>2</sub>	% H <sub>2</sub>	% CH <sub>4</sub>	Soil moisture	Topography	Surface water	Obliquity
05H0	0.5	89	0	1	Dry	Modern	None	25.19°
05H3	0.5	86	3	1	Dry	Modern	None	25.19°
1H0	1	89	0	1	Dry	Modern	None	25.19°
1H3	1	86	3	1	Dry	Modern	None	25.19°
AK1	1	97	3	0	Dry	Modern	None	25.19°
RW1	1	94	5	1	Dry	Modern	None	25.19°
1H6	1	83	6	1	Dry	Modern	None	25.19°
RH1	1	90	10	0	Dry	Modern	None	25.19°
15H0	1.5	89	0	1	Dry	Modern	None	25.19°
15H3	1.5	86	3	1	Dry	Modern	None	25.19°
15H5	1.5	94	5	1	Dry	Modern	None	25.19°
AK15	1.5	97	3	0	Dry	Modern	None	25.19°
RH15	1.5	90	10	0	Dry	Modern	None	25.19°
2H0	2	89	0	1	Dry	Modern	None	25.19°
2H3	2	86	3	1	Dry	Modern	None	25.19°
AK2	2	97	3	0	Dry	Modern	None	25.19°
RW2	2	94	5	1	Dry	Modern	None	25.19°
RW2wet	2	94	5	1	Wet	Modern	None	25.19°
RH2	2	90	10	0	Dry	Modern	None	25.19°
RW2lakes	2	94	5	1	Wet	Modern	10 m GEL Lakes	25.19°
RW2lakeso0	2	94	5	1	Wet	Modern	10 m GEL Lakes	0°
RW2lakeso45	2	94	5	1	Wet	Modern	10 m GEL Lakes	45°
RW2lakes100	2	94	5	1	Wet	Modern	100 m GEL Lakes	25.19°
RW2lakes100o0	2	94	5	1	Wet	Modern	100 m GEL Lakes	0°
RW2lakes500	2	94	5	1	Wet	Modern	500 m GEL Lakes	25.19°
RW2TPWlakes	2	94	5	1	Wet	Paleo	10 m GEL Lakes	25.19°
RW2TPWlakeso0	2	94	5	1	Wet	Paleo	10 m GEL Lakes	0°
RW2TPWlakeso45	2	94	5	1	Wet	Paleo	10 m GEL Lakes	45°
RW2TPWlakes100	2	94	5	1	Wet	Paleo	100 m GEL Lakes	25.19°
RW2TPWlakes100o0	2	94	5	1	Wet	Paleo	100 m GEL Lakes	0°
RW2TPWlakes500	2	94	5	1	Wet	Paleo	500 m GEL Lakes	25.19°
NHOcean	2	94	5	1	Wet	Modern	Ocean	25.19°
HOcean	2	94	5	1	Wet	Modern	Ocean	25.19°

basaltic surfaces. Some simulations (detailed below) use a possible paleotopography (Table 1) shown by Bouley et al. (2016) (see also Matsuyama & Manga, 2010) before the development of the Tharsis Montes and associated true polar wander (TPW). All simulations use an “active lakes” capability of ROCKE-3D (also used for ancient Venus by Way et al., 2016) where the model can produce bodies of surface liquid water based on runoff and precipitation patterns. In some simulations, we initialize the model with existing surface liquid water as “lakes” in topographic low points such as Hellas basin, deep craters, and the northern lowlands. The model simulates an active water cycle with frozen and liquid precipitation, deposition of snow on the surface, and surface runoff. We also conduct two simulations with fully dynamic oceans. In these simulations, the ocean is “spun up” from rest much like the atmosphere. For lack of better alternatives, the ocean model uses modern Earth ocean salinity and mesoscale eddy parameterizations. Del Genio

et al. (2019) thoroughly describes ROCKE-3D's ocean model and the reader is referred to that work for additional details.

Clouds and atmospheric convection are discussed in detail in Way et al. (2017) and only H<sub>2</sub>O clouds are included in our simulations. In brief, the model uses the cumulus parameterization of Del Genio et al. (2015). The scheme uses a penetrative mass flux approach in which the buoyancy of a lifted air parcel determines convective onset, entrainment of drier environmental air determines the loss of buoyancy and eventual cloud top, detrainment of water vapor and ice near cloud top moistens the upper levels, and compensating subsidence dries the surrounding environment. This version of ROCKE-3D uses the "AR5" generation of the parameterization, described in more detail in Del Genio et al. (2015). That version entrains less than it should, but given the dry conditions through most of Mars' troposphere (see e.g., Figure 9 below), convection has little impact on the simulations. As discussed more in Section 3, there are limited convective clouds in our simulations, but unlike Earth, where the very warm tropical oceans spawn extensive deep convection and precipitation and organize the large-scale circulation, oceans in our Mars simulations are cooler than the same regions in simulations without oceans and have no deep convection. Instead, deep convection occurs preferentially in localized areas of high topography and to a smaller extent scattered around the rest of the planet for the wetter simulations.

Cirrus (H<sub>2</sub>O ice) cloud properties are parameterized following Edwards et al. (2007) and are assumed to be Mie scatterers. Note the model does not include CO<sub>2</sub> ice in the atmosphere or on the surface, even if the temperature falls below the frost point. Some ancient Mars climate studies have suggested that CO<sub>2</sub> ice clouds may play an important role in warming the planet's surface (Forget et al., 2013; Forget & Pierrehumbert, 1997; Wordsworth et al., 2013). CO<sub>2</sub> cloud physics are in development for ROCKE-3D and their impacts will be examined in future work. As Mars' ubiquitous dust was likely formed after any wet climate period (e.g., Pike et al., 2011), dust is not included in the simulations.

Our simulations are all run until they reach radiative equilibrium. Simulations that are initialized with "dry" soil (and thus have minimal, but nonzero, global water inventory) are run for 20 Mars years with the final year used for results below. Simulations initialized with "wet" soil or with surface liquid water are run until they both reach radiative and hydrological equilibrium. Evaluating hydrological equilibrium is discussed below. In practice, hydrological equilibrium requires ~500 Mars years of model run time with modern topography and 2000 years or more for the paleotopography.

All our simulations are listed in Table 1. Any gas mixtures that do not sum to 100% include the remaining percent as N<sub>2</sub>. Simulations with initialized surface water are presented as the total volume (in global equivalent layer, GEL) and whether the water was initialized as lakes or oceans in the model.

### 3. Results

We group our simulations into two categories: those initiated with no surface liquid water and either dry or wet soil and those initiated with some inventory of surface liquid water. We use the first group, which we generally term as "dry" simulations, to find gas mixtures and surface pressure values that are supportive of surface liquid water to use in the "wet" simulations (those initiated with surface liquid water).

#### 3.1. Dry Simulations

Our dry simulations all use surface pressures between 0.5 and 2 bar at intervals of 500 mb with a variety of gas mixtures. All simulated atmospheres have 83%–94% CO<sub>2</sub>, 0%–6% H<sub>2</sub>, 1% CH<sub>4</sub>, and any remainder to reach 100% is N<sub>2</sub> (with the exception of the simulations detailed below that use gas mixtures described in the literature). H<sub>2</sub>O is treated as a trace gas in all simulations and is not assumed to ever make a substantive change to the mean molecular weight of the atmosphere. In most of our "dry" simulations, the atmosphere has no water vapor at the beginning of the simulation and there is a small amount of soil moisture. In a small subset of these simulations, there is a larger amount of initialized soil moisture.

We also conducted a series of simulations with gas mixtures and pressures described in the literature for purposes of model intercomparison and to help put our results into context relative to the existing literature on ancient martian climate, particularly more recent work that looks at the role of reducing greenhouse

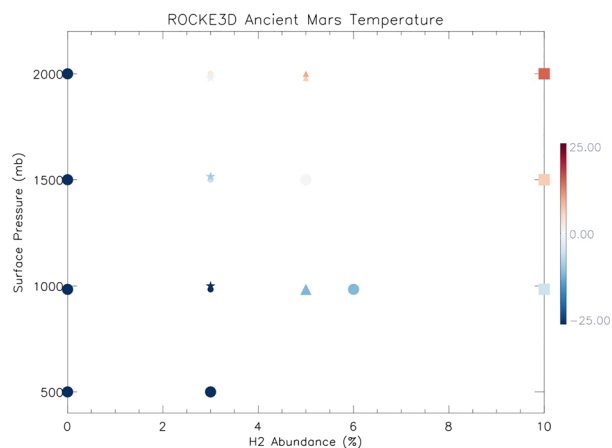


**Figure 3.** Global mean annual surface temperatures (°C) of “dry” ROCKE-3D simulations as a function of surface pressure and H<sub>2</sub> abundance. Our gas mixtures are identified with circles, squares represent simulations using gas mixtures described by Haberle et al. (2019), stars represent simulations using Kamada et al. (2020) gas mixtures, and triangles represent Wordsworth et al. (2017) gas mixtures. Some simulations with similar surface pressures and H<sub>2</sub> abundances are indicated with smaller symbols and slightly offset in pressure for clarity.

gases and CIA. Specifically, we simulate some of the gas mixtures and pressures of Wordsworth et al. (2017), Kamada et al. (2020), and Haberle et al. (2019). Wordsworth et al. (2017) used 94% CO<sub>2</sub>, 5% H<sub>2</sub>, and 1% CH<sub>4</sub> with surface pressures of 1- or 2-bar. Kamada et al. (2020) used 97% CO<sub>2</sub> and 3% H<sub>2</sub> (among others, but found some amount of seasonal melting began at that point) and we simulated that gas mixture with surface pressures of 1-, 1.5-, and 2-bar. Haberle et al. (2019) used 90% CO<sub>2</sub> and 10% H<sub>2</sub> (again, among others) and that was, again, simulated with surface pressures of 1-, 1.5-, and 2-bar.

Figure 3 shows global mean annual surface temperatures of 19 ROCKE-3D simulations. A couple of conclusions are immediately apparent from looking at Figure 3. First, without H<sub>2</sub> (and the associated CIA), even 2-bar, pure CO<sub>2</sub> surface pressures are insufficient to produce global mean annual surface temperatures above the freezing point of water. In fact, the 2 bar 0% H<sub>2</sub> simulation (Simulation 2H0 from Table 1) has a global mean annual surface temperature of  $-29.1^{\circ}\text{C}$ . This is substantially warmer than a comparable atmosphere and pressure presented in Forget et al. (2013), possibly due to the lack of CO<sub>2</sub> condensation in ROCKE-3D which would serve to warm the middle atmosphere. Increasing H<sub>2</sub> abundance to 3%–5% produces temperatures near freezing or slightly above freezing for Simulations 2H3, RW2, and AK2. The other immediate conclusion from Figure 3 is that 1-bar surface pressure is insufficient for global mean annual surface temperatures above freezing in ROCKE-3D simulations, even with H<sub>2</sub> abundances of 10% as in Simulation RH1.

Compared to the published results that we have used as guidance for some gas mixtures and pressures, we find generally good agreement. Wordsworth et al. (2017) used a line-by-line spectral code to evaluate the climate impact of their *ab initio* calculations of CIA and found that CO<sub>2</sub>-H<sub>2</sub> mixtures reached 0°C with approximately 3% H<sub>2</sub> for 2-bar pressures and 5% H<sub>2</sub> at 1.5-bar pressures. Adding CH<sub>4</sub> reduced the amount of H<sub>2</sub> necessary for above-freezing conditions. As seen in Table 1, our simulations following Wordsworth et al. (2017) (RW simulations) all have 1% CH<sub>4</sub> and 5% H<sub>2</sub>. The resulting global mean annual surface temperatures are quite comparable to those shown by Wordsworth et al. (2017), with Simulation RW1 having a temperature of  $-24.5^{\circ}\text{C}$ , Simulation RW2 having a temperature of  $14.0^{\circ}\text{C}$ , and Simulation RW2wet (with higher initial soil moisture) having a temperature of  $15.7^{\circ}\text{C}$ . The slightly warmer temperature for wetter soil conditions is due to the higher water vapor amounts in the atmosphere. Haberle et al. (2019), extrapolating from the 1D model of Wordsworth et al. (2017), found that large impacts of iron-rich meteorites could degas substantial H<sub>2</sub> and that mixing ratios of 10% or more produce temperatures above 0°C for 1-bar or thicker atmospheres. Our 1-bar simulation, Simulation RH1 (90% CO<sub>2</sub> & 10% H<sub>2</sub>), has a global mean annual surface temperature of  $-13.5^{\circ}\text{C}$ , but the simulations with thicker atmospheres, Simulations RH15 and RH2, have temperatures of  $8.5^{\circ}\text{C}$  and  $23.9^{\circ}\text{C}$ , respectively. Our generally good match to Wordsworth et al. (2017) at 1-bar and poorer match to Haberle et al. (2019) suggests that 3D simulations are needed to account for additional effects such as cloud albedo (e.g., Figure 7). Our simulations following Kamada et al. (2020) are similar to their “Dry-Mars” simulations with 3% H<sub>2</sub> and result in temperatures quite similar to theirs, with all three simulations (Simulations AK1, AK15, and AK2) having global mean annual surface temperatures below freezing. Indeed, on balance, our simulation temperatures compare quite favorably with the “Dry-Mars” simulations by Kamada et al. (2020), even for other mixing ratios of H<sub>2</sub>, and accounting for their higher (our lower) mixing ratios of CO<sub>2</sub> and our inclusion of 1% CH<sub>4</sub>.

In Figures 4 and 5, we take a global view to see how temperatures vary. The same points discussed with Figure 3 generally continue to hold. Namely, even at 1-bar surface pressures, most or all of the planet sees annual average temperatures below freezing. With 5%–6% H<sub>2</sub>, small regions of Hellas Basin see above freezing annual average temperatures. Increasing that to 10% H<sub>2</sub> in Simulation RH1 expands that to portions of the northern hemisphere lowlands. Second, some amount of H<sub>2</sub> is necessary to have any portion of the planet experience annual average temperatures above the freezing point of water. Simulation 2H0 (bottom

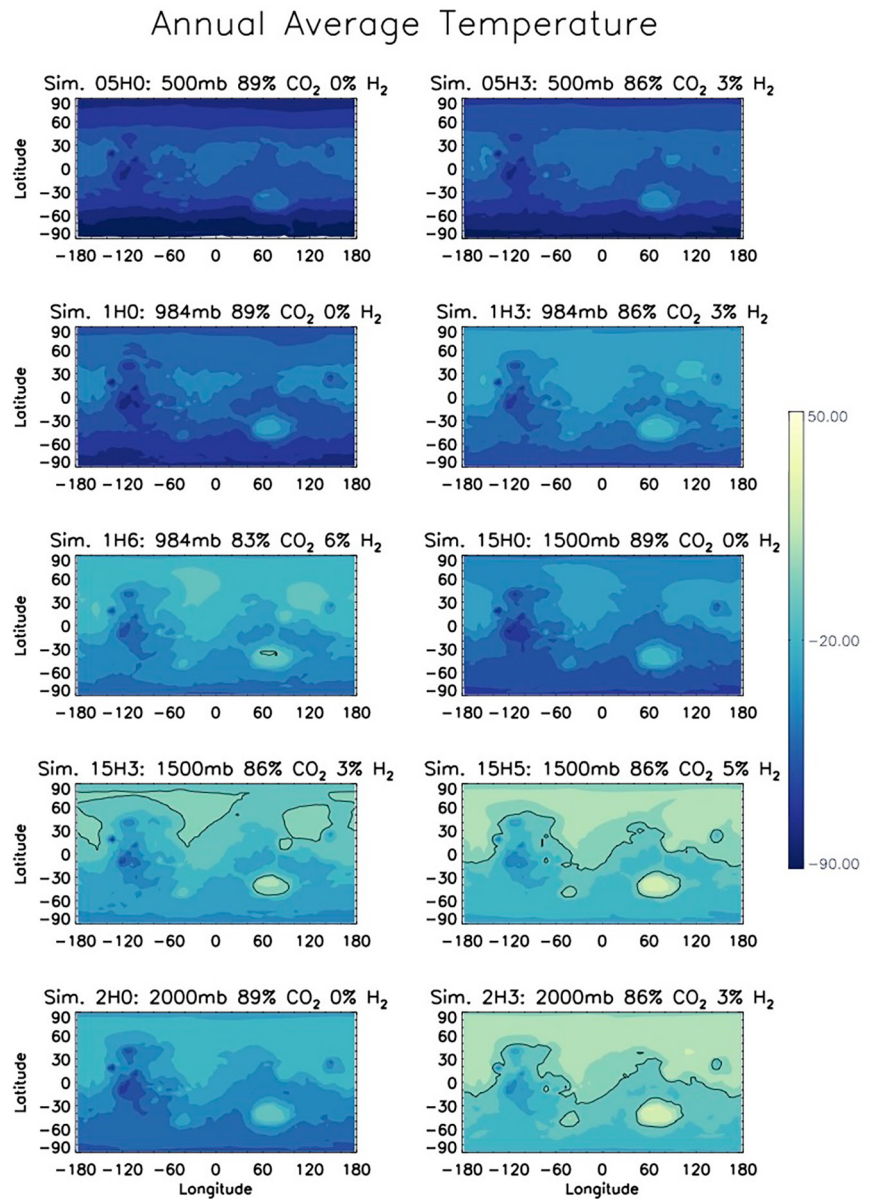


**Figure 4.** Mean annual surface temperatures ( $^{\circ}\text{C}$ ) for 10 ROCKE-3D simulations with surface pressures and  $\text{CO}_2$  and  $\text{H}_2$  mixing ratios identified in the panel title. All simulations incorporate dry soil. The black line indicates the freezing point of water.

left panel of Figure 4) shows no regions of the planet above freezing despite a 2-bar atmosphere of  $\text{CO}_2$ . All planets with global mean annual average temperatures above  $-25^{\circ}\text{C}$  have some region of the planet above freezing on an annual average basis. Simulations with increasing surface pressure and  $\text{H}_2$  amounts eventually reach a point where most of the planet is above freezing (e.g., Simulation RH2) although the high elevations of the Tharsis Montes and plateau remain below freezing in all simulations. This is particularly relevant for cold-trapping of water, as will be discussed below.

Not surprisingly, but worth mentioning, is that the regions that preferentially experience above freezing annual average temperatures are the topographic low spots in Hellas Basin and the northern lowlands. The gradient in temperature with topography is due to adiabatic effects (Wordsworth et al., 2013), which modern Mars does not experience due to its thin atmosphere. These are not the locations that have the highest density of valley networks and outflow channels, which fall near the topographic dichotomy boundary and



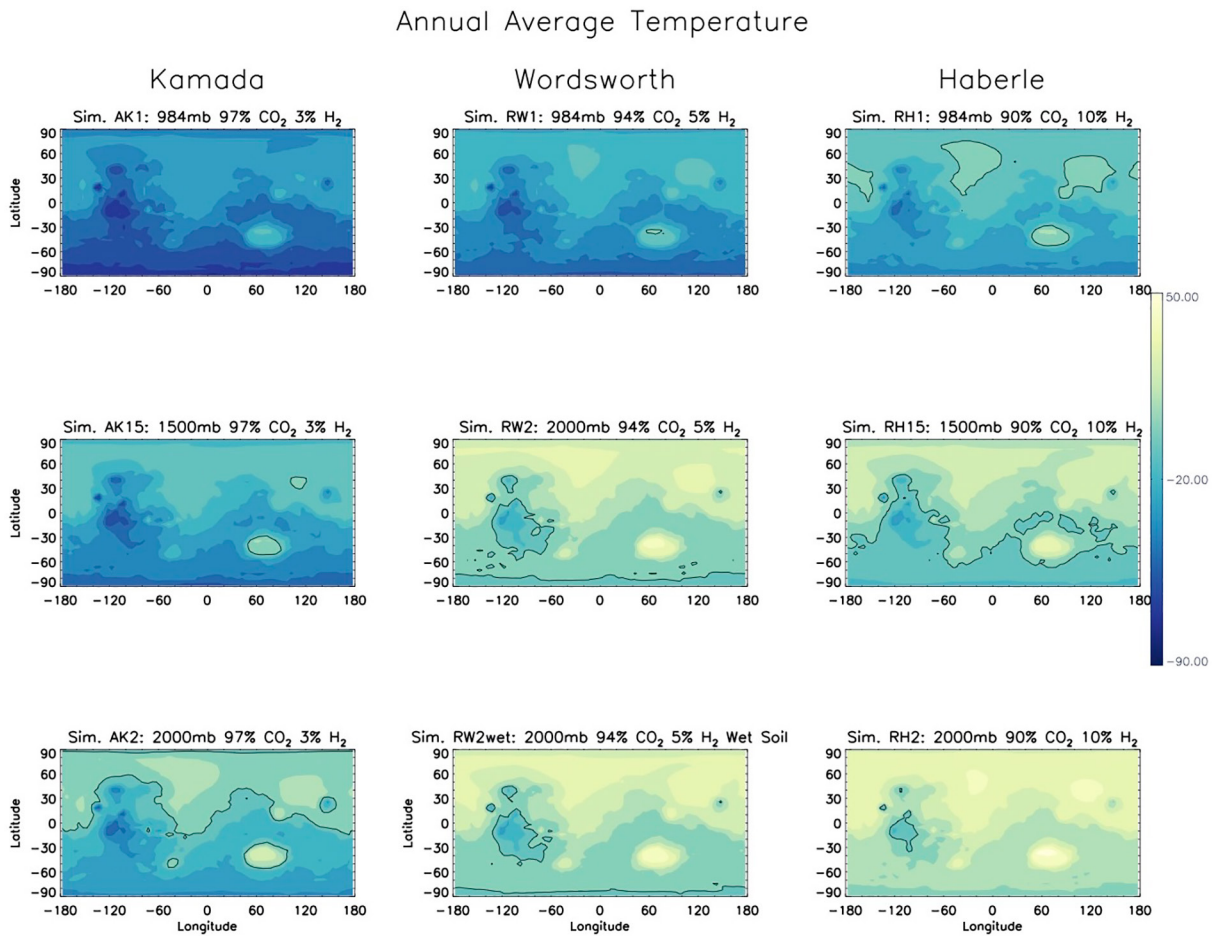


**Figure 5.** Same as in Figure 4, except for gas mixtures described in the literature as delineated above.

in the southern hemisphere highlands (Hynek et al., 2010). This disparity is well-known from studies of possible ancient martian climates (e.g., Palumbo & Head, 2018).

Looking at seasonal temperatures, we see in Figure 6 that 1-bar (with some H<sub>2</sub> present in the atmosphere) or higher-pressure simulations all have some regions of the planet with portion of the year with hourly minimum temperatures above freezing, again, predominantly in Hellas basin or the northern lowlands. In the highest pressure and H<sub>2</sub> mixing ratio, and thus warmest, simulations (bottom right two panels of Figure 6) the northern lowlands and Hellas basin are above freezing year-round. Interestingly, however, even parts of the southern hemisphere highlands (e.g., Aonia Terra and Terra Sirenum, both south of the Tharsis plateau) experience seasonally warm temperatures and some of those regions do exhibit high density of valley networks as shown by Hynek et al. (2010). That is also true of areas near the topographic dichotomy boundary in the eastern hemisphere, although the Terra Sabaea and Tyrrhena Terra regions (both with numerous valley networks) north of Hellas remain below freezing all year.

As stated above, our “dry” simulations (nearly) all use initial soil moisture conditions that have a small amount of water present in the soil that is then moved through the climate system following the water cycle parameterizations in the GCM. Despite the comparatively small amount of water (relative to the simulations described below in Section 3.2) in the system, the simulations do produce water cloud cover. Even for modern terrestrial climate studies, understanding the complete climatic influence of clouds remains an area of ongoing research and much work has been done regarding how clouds (both H<sub>2</sub>O and CO<sub>2</sub>) may have impacted the ancient climate of Mars (e.g., Forget et al., 2013).

% of Year with Above Freezing Minimum Temperature

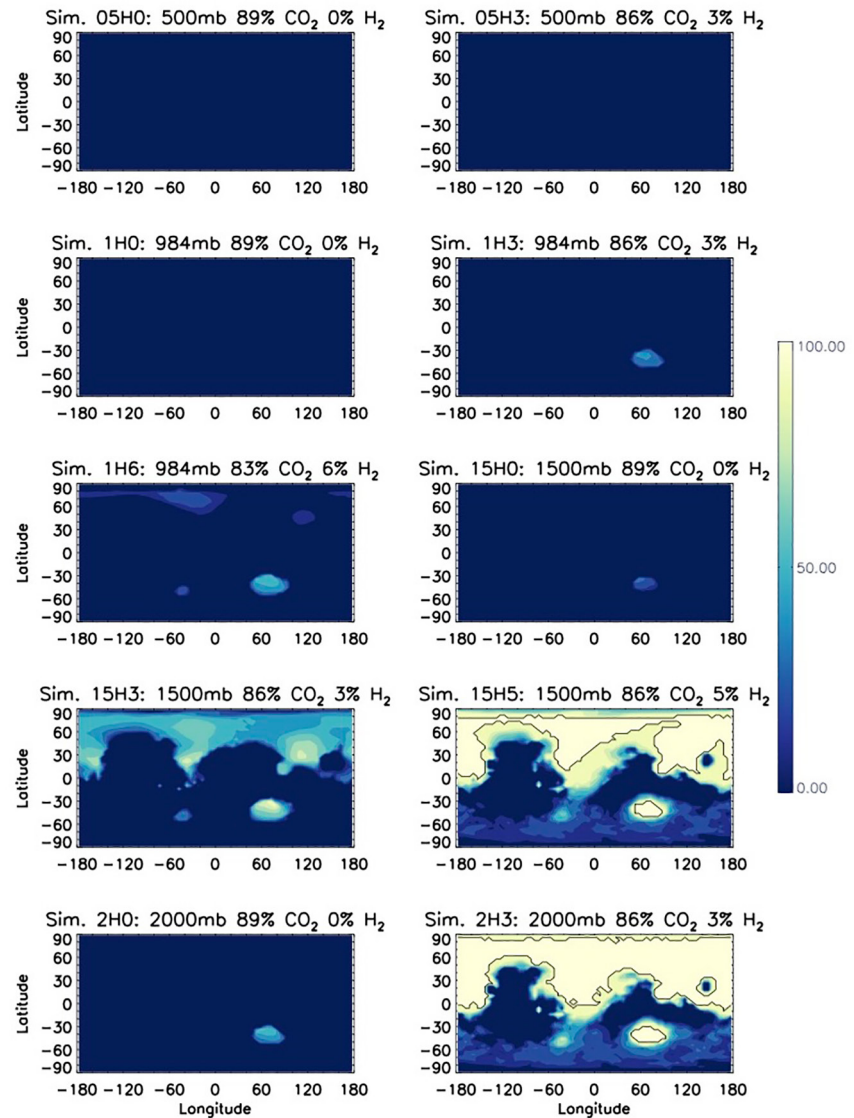


**Figure 6.** Percent of the year with above freezing hourly minimum temperatures for 10 ROCKE-3D simulations with surface pressures and CO<sub>2</sub> and H<sub>2</sub> mixing ratios identified in the panel title. All simulations incorporate dry soil. The black line encloses the areas with 100%.

Figure 7 shows that substantial clouds are found in the tropics. Although some convective-type clouds occur over Tharsis, the bulk of the clouds are thin, cirrus-like water ice clouds. The coldest simulations (low pressure and lower H<sub>2</sub> mixing ratios) have generally clear atmospheres, with infrequent tropical clouds as well as seasonal clouds over the south pole. Warmer simulations (high pressure and higher H<sub>2</sub> mixing ratios) have a well-defined tropical cloud belt between 30°S and 30°N with little longitudinal variation. Some simulations (e.g., Simulation 2H0, bottom left panel of Figure 7) additionally suggest that Hellas basin sees some amount of cloud cover, which is true even in the modern climate.

The depiction of clouds in the dry simulations is more complicated than seen in Figure 7, however, as shown in Figure 8. Whereas the 1-bar simulations in Figure 7 all have generally clear atmospheres, Figure 8 shows that Simulations AK1 and RH1 are much cloudier, more so even than the 2-bar simulations in Figure 7. In all cases (Figures 7 and 8), the clouds depicted are thin cirrus-like water ice clouds and have peak ice mixing ratios in the 100–200 mb pressure range (see also Figure 9). Despite their broad coverage, they

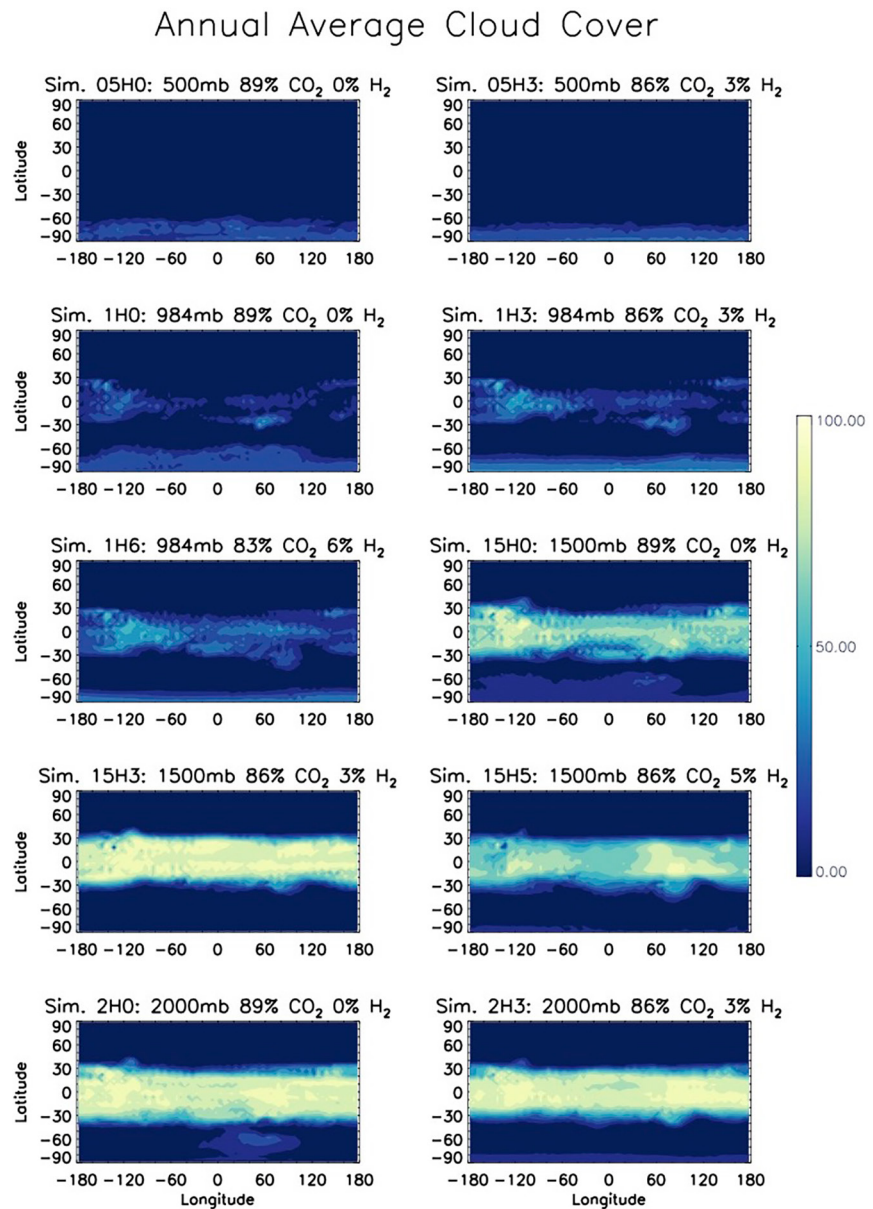


**Figure 7.** Annual-average cloud cover for 10 ROCKE-3D simulations with surface pressures and CO<sub>2</sub> and H<sub>2</sub> mixing ratios identified in the panel title. All simulations incorporate dry soil and 1% CH<sub>4</sub> in their atmospheres.

have minimal net radiative effect ( $\sim O(1)$  W/m<sup>2</sup>). Indeed, even the few areas of convective clouds (predominantly over Tharsis) only have longwave and shortwave cloud radiative forcings of  $\sim 3$  W/m<sup>2</sup>.

The pattern of the Kamada and Haberle simulations being both much cloudier than the Wordsworth simulations and those in Figure 7, even when adding in a wetter soil moisture initial condition (Simulation RW2wet, bottom center panel of Figure 8), continues at higher pressures as well. The reason is ultimately their disparate atmospheric gas compositions. All simulations in Figure 7 and the Wordsworth simulations in Figure 8 all include 1% CH<sub>4</sub>. As shown by Bryne and Goldblatt (2015) for the Archean Earth, 0.1% and higher mixing CH<sub>4</sub> ratios facilitate strong shortwave absorption in the troposphere and stratosphere. Wordsworth et al. (2017) also saw this higher-altitude warming from CH<sub>4</sub>. This stronger shortwave absorption is reflected in the most recent updates of the HITRAN database that ROCKE-3D uses (e.g., Brown et al., 2013; Rothman et al., 2013), but was not reflected in earlier versions. Higher CH<sub>4</sub> mixing ratios produce sufficient absorption to create a distinct tropopause, and this is precisely what we see when looking

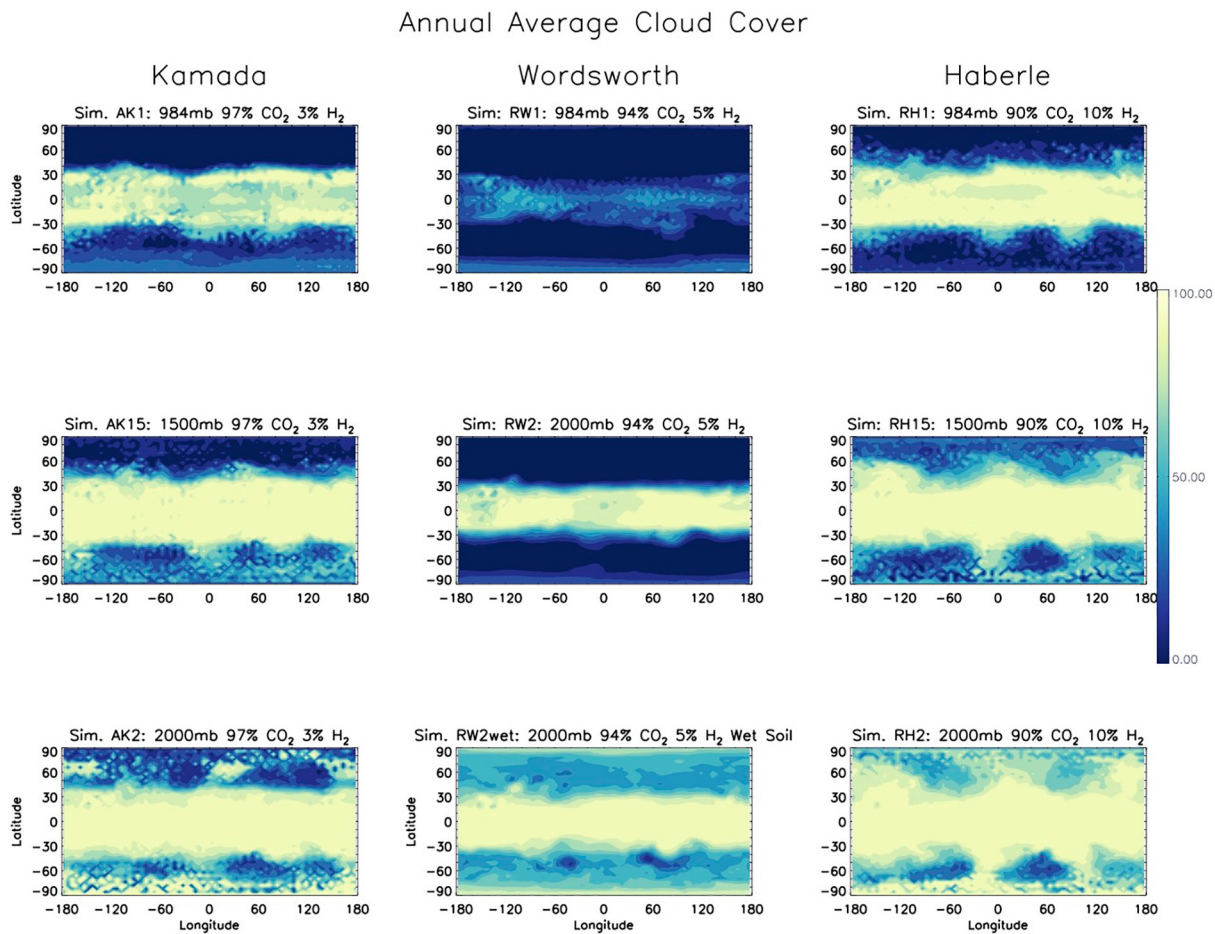


**Figure 8.** Same as in Figure 7, except for gas mixtures described in the literature as denoted above. Wordsworth simulations include 1% CH<sub>4</sub>.

at our simulations (Figure 9). Despite higher specific humidities in the Wordsworth simulations and those in Figure 7, the warmer upper tropospheric temperature and reduced tropospheric relative humidity limit the cloud production (see Figure 9), relative to the Kamada (AK1) and Haberle (RH1) simulations without CH<sub>4</sub>. Increased static stability limiting cloud production in our simulations with CH<sub>4</sub> is analogous to similar studies of Archean Earth that removed O<sub>2</sub> and O<sub>3</sub> and noted this resulted in decreased cloud production (e.g., Wolf & Toon, 2013).

From the perspective of these simulations, the difference in cloud cover is ultimately due to warmer upper tropospheric temperatures. In all variables relevant to cloud production, the simulations without CH<sub>4</sub> are distinct from simulations with it (Figure 9). Simulations AK1 and RH1, without CH<sub>4</sub>, exhibit cooler upper tropospheric temperatures and produce both thicker and more widespread cloud cover. Despite the simulations with CH<sub>4</sub> having a distinct tropopause, the temperature inversion is weak and water is not substantially cold-trapped. Indeed, specific humidity values only slightly reflect the temperature inversion in the simulations with CH<sub>4</sub> (Figure 9). This “leaky” tropopause is similar to that on Titan, where CH<sub>4</sub> still mixes into the stratosphere and mesosphere and is eventually photodissociated and destroyed (e.g., Roe, 2012). Indeed, a hygropause is more efficiently produced by the thick cloud cover preventing vertical water transport (see Simulation AK1 in Figure 9). Water ice clouds also limit vertical water transport in the modern martian climate system (Clancy et al., 1996; Navarro et al., 2014). This result suggests that comparatively subtle features such as trace gas mixing ratios (i.e., CH<sub>4</sub> in this case) and cloud cover may have been important for water loss in the early martian climate system.

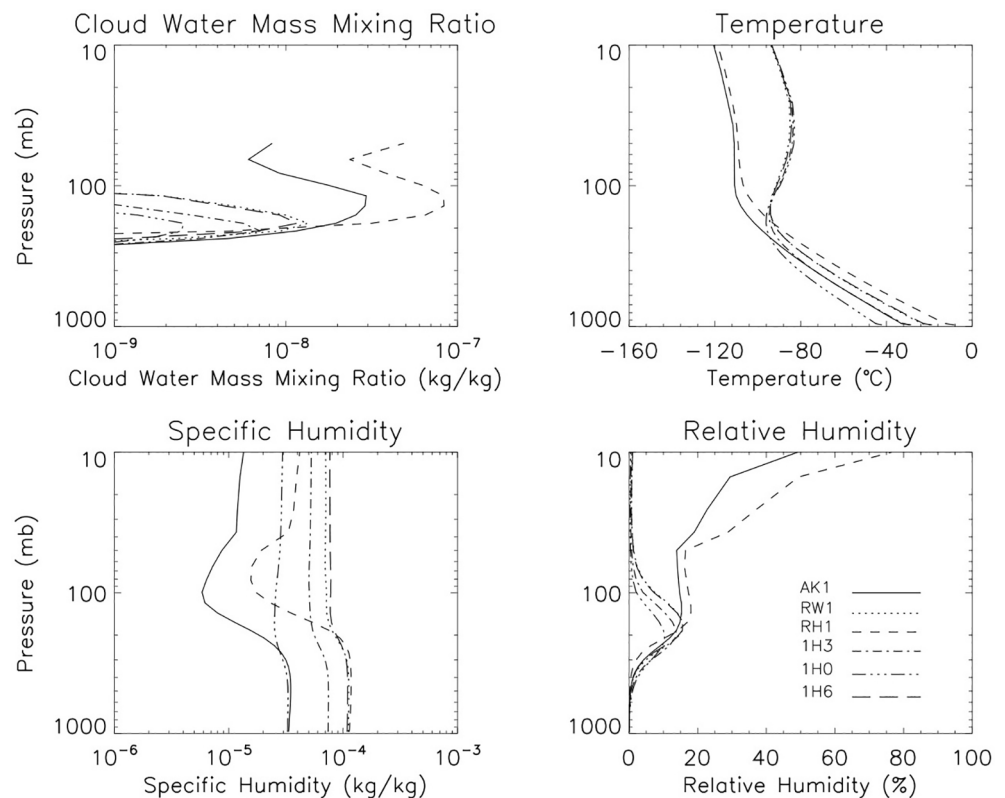


**Figure 9.** Average vertical profiles of cloud mass mixing ratio, temperature, specific humidity, and relative humidity for the 30°S–30°N latitude band for 6 ROCKE-3D simulations (as identified in the relative humidity panel).

### 3.2. Wet Simulations

Our next set of simulations are initialized with surface liquid water in the form of active lakes. Those lakes are then depleted or replenished based on the precipitation and evaporation patterns within the simulation. The first set of these “wet” simulations uses the RW2 simulation gas mixture (94% CO<sub>2</sub>, 5% H<sub>2</sub> & 1% CH<sub>4</sub>) and modern topography. Each simulation is run until hydrological equilibrium is reached, which always takes much longer than radiative equilibrium. We define hydrological equilibrium as the point where hydrological variables (e.g., mass of water in lakes, mass of ground water, mass of ground ice, snow depth, and ocean ice fraction) are in steady-state.

Using modern topography, hydrological equilibrium is always reached with all lakes on the planet being completely depleted and the remaining water in the climate system consisting of surface and subsurface snow and ice and ground water. This is due to the cold trapping of nearly all the planet’s water on Tharsis, and, to a lesser degree, the south pole. Wordsworth et al. (2015) also describe this cold-trapping at Tharsis and the poles with modern topography (see also Palumbo & Head 2018). The annual precipitation patterns for this first set of six simulations is shown in Figure 10. The heaviest precipitation consistently falls on the upwind (westward) side of Tharsis, particularly Arsia Mons, for every simulation except those with 0° obliquity. In fact, the maximum total annual precipitation (707 mm) occurs in the RW2lakes simulation (upper left panel of Figure 10), with only 10 m of GEL water.

In simulations with modern obliquity or 45° obliquity, there is a prominent rain shadow east of Tharsis (see also Wordsworth et al., 2015). Comparing with Figure 11, which only shows liquid precipitation, indicates that much of the precipitation that falls over Tharsis and the south pole falls as snow. However, the simulations with 0° obliquity are distinctly different (middle two panels of Figures 10 and 11). Simulations with 0° obliquity show much more widespread precipitation, with precipitation on both sides of Tharsis, across the topographic dichotomy boundary and through the southern highlands. Maximum precipitation at a given location (also in Tharsis) is somewhat less, however, at ~500 mm per year. Notably, the simulations

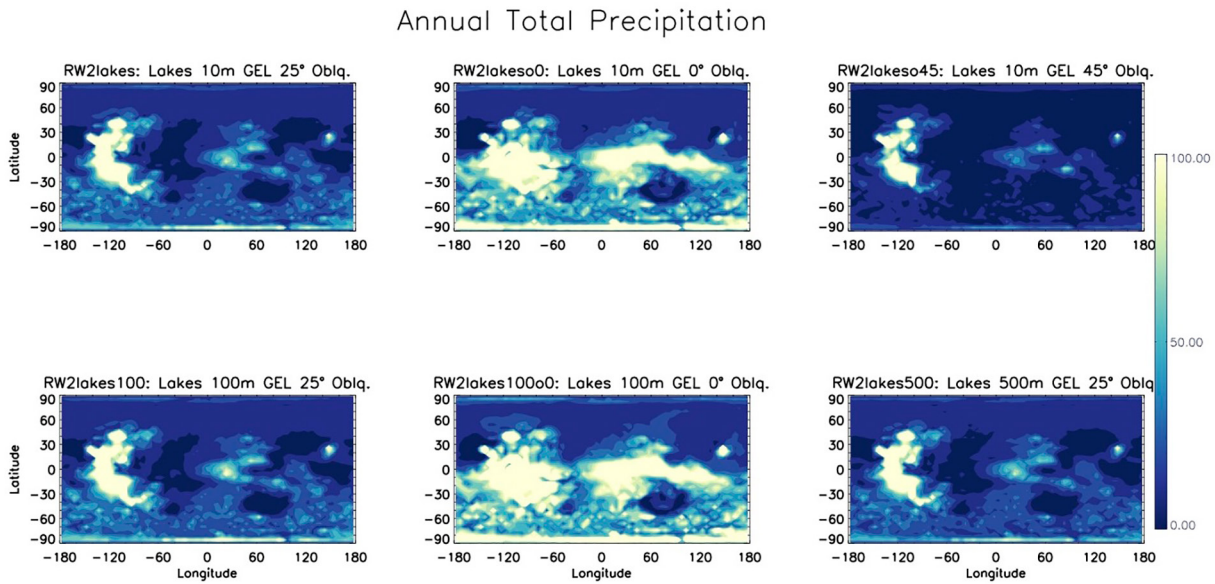


**Figure 10.** Annual total precipitation (mm) for 6 ROCKE-3D simulations distinguished by total initial water inventory and obliquity. All water is initialized in lakes and then moved through the climate system.

with 0° obliquity have much more *liquid* precipitation than those with 25° or 45° and it is fairly evenly distributed across the low and middle latitudes including across locations with valley network formations (Hynek et al., 2010).

Simulations with modern or 45° obliquity show little precipitation in areas with valley network formations, regardless of the planet's initial water inventory. In fact, the simulation with 45° obliquity (often suggested to be a “warmer” climate state in the literature [Palumbo & Head, 2018]) is the driest simulation over the southern highlands where valley networks are seen. However, note again that the 0° obliquity simulations experience substantially more rainfall with a broader distribution than either 25° or 45° obliquity simulations. Again, there is minimal change to precipitation in the 0° obliquity simulations based on initial water

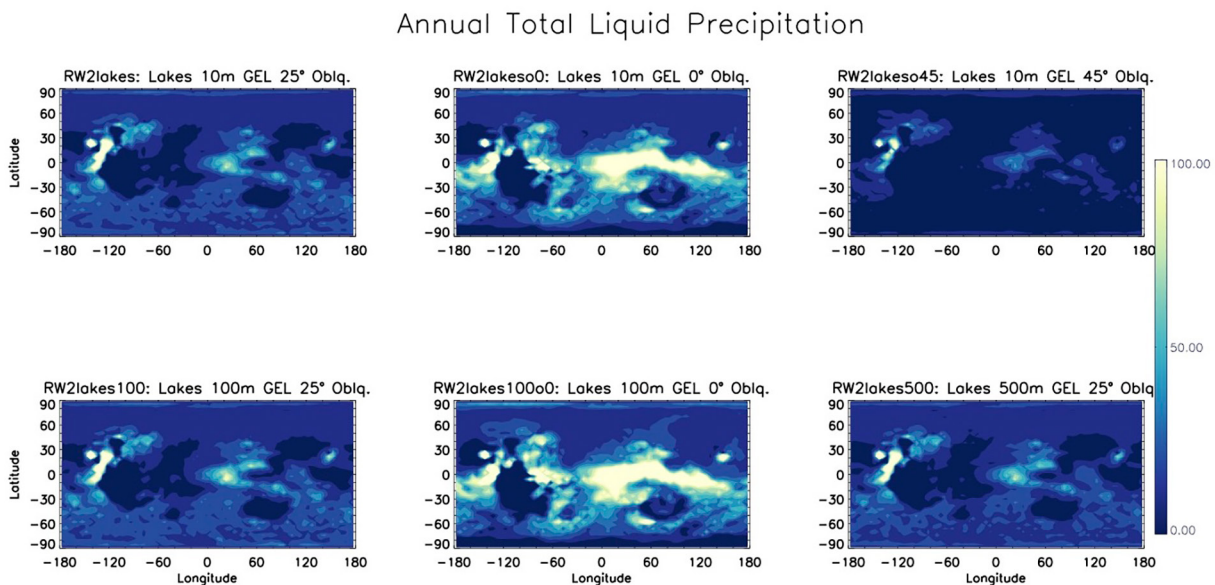


**Figure 11.** Same as Figure 10 except for annual total liquid precipitation (mm).

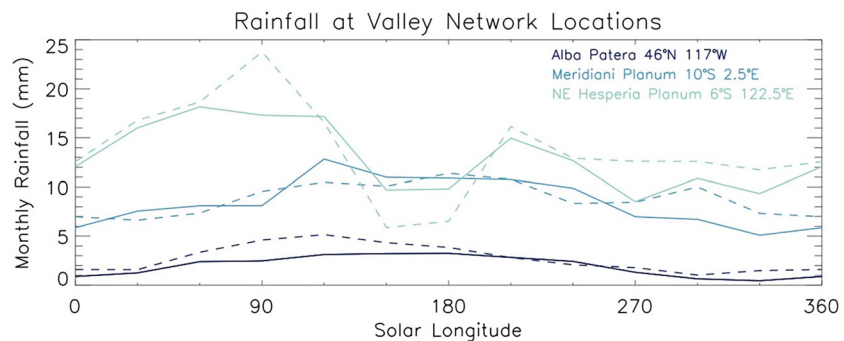


**Figure 12.** Simulated annual rainfall at three locations with high drainage density per Hynek et al. (2010). Solid lines indicate simulation RW2lakes00 with 10 m GEL initial water inventory and dashed line indicates simulation RW2lakes100o0 with 100 m GEL initial water inventory. Locations are specified in the figure.

inventory, but there is a slight increase with 100 m GEL (bottom middle panel of Figures 10 and 11) relative to the 10 m GEL simulation (top middle panel of Figures 10 and 11).

Recall this version of ROCKE-3D does not have CO<sub>2</sub> condensation physics, as mentioned above, but annual minimum temperatures in this simulation are well above the CO<sub>2</sub> frost point (typically  $-35^{\circ}\text{C}$  to  $-25^{\circ}\text{C}$  in the coldest location in the Tharsis Montes) at all locations on the surface and the obliquity drives minimal seasonal variation. Our simulations show that  $0^{\circ}$  obliquity is the most plausible for producing rainfall and associated runoff and erosion capable of creating the valley network formations. We show this in more detail in Figure 12. We plot “monthly” ( $\sim 30^{\circ}$  of solar longitude) rainfall using three sample areas from Hynek et al. (2010) that have high drainage density across the planet. All three locations show modest rainfall throughout the martian year. As stated above, increasing the initial water inventory of the planet does not substantially alter the final hydrological balance when the simulations use modern topography. Note, however, that there is not perfect congruence between valley network formation locations and predicted rainfall in our simulations with  $0^{\circ}$  obliquity. For example, locations south of Tharsis such as the highlands of Solis Planum, see near-zero rainfall in our simulations. Those locations such as Solis Planum do see snowfall, however, and annual average temperature there is near freezing, so some seasonal melting is plausible. Episodic snowmelt and runoff is another plausible formation mechanism for some valley network formations (e.g., Palumbo et al., 2020; Wordsworth et al., 2015).

Our second set of “wet” simulations also uses the RW2 simulation gas mixture, but uses an inferred topographic map before the formation of Tharsis and associated true polar wander. We use the map from Bouley et al. (2016) (see also Matsuyama & Manga, 2010). The timing of the formation of Tharsis relative to the formation of the valley networks and lake systems on Mars is critical for understanding the plausible climate of the late Noachian (also see Citron et al. (2018) regarding putative ocean shorelines as it relates to Tharsis formation). The lack of Tharsis to serve as a strong cold trap produces a much more robust hydrological cycle. Using the assumed paleotopography, annual mean surface temperatures are comparable or slightly cooler (1–2 K) than the same simulation using modern topography (Figure 13). However, the coldest mean annual surface temperatures on the planet are  $\sim 10^{\circ}\text{C}$  warmer in the paleotopography simulations. This is sufficient to prevent the extreme cold trapping of water that is seen on the Tharsis plateau when using modern topography. Additionally, because water is not as extensively cold trapped, and more is actively circulating hydrologically, the global mean surface temperature is slightly dependent on the initial water inventory. Simulations initialized with 100 m or 500 m GEL water inventories are 5–9°C colder than equivalent simulations with 10 m GEL initial water inventory. This is due to increased snow and ice coverage and more widespread clouds in simulations with greater water inventories. Notably, the simulations with  $0^{\circ}$  obliquity are, again, the warmest. For example, the three simulations with 10 m GEL water inventory and obliquities of  $0^{\circ}$ ,  $25.19^{\circ}$ , and  $45^{\circ}$  have global annual mean surface temperatures of:  $13^{\circ}\text{C}$ ,  $11.8^{\circ}\text{C}$ , and  $9.9^{\circ}\text{C}$ , respectively.

Assuming the valley networks formed prior to Tharsis formation and associated true polar wander, they would be placed in an east-west oriented band centered in the southern low latitudes near  $24^{\circ}\text{S}$  (Bouley

Paleo Topography Annual Average Temperature

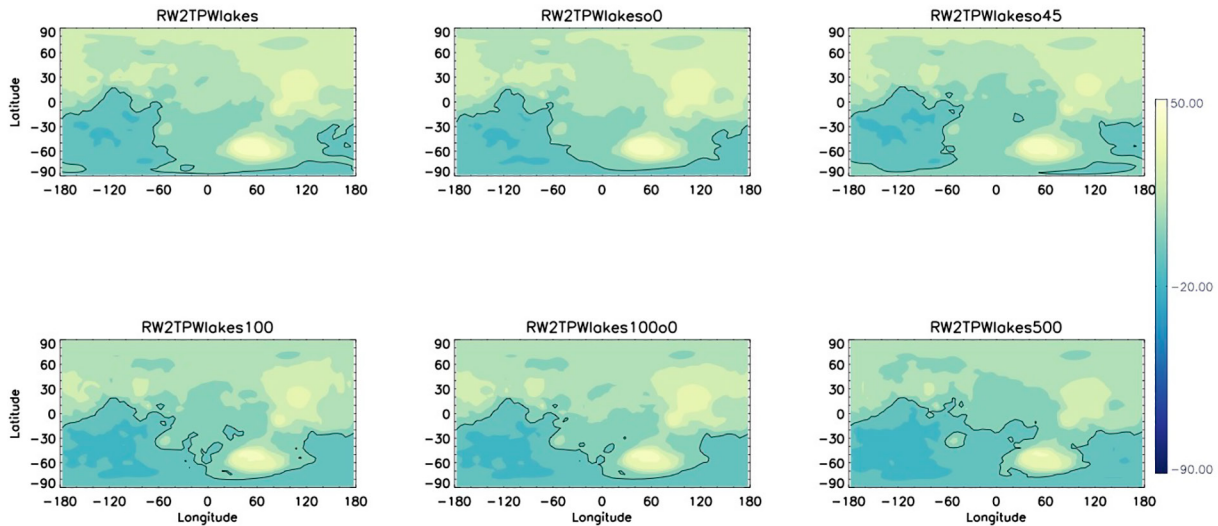


**Figure 13.** Mean annual surface temperatures (°C) for 6 ROCKE-3D simulations using the martian paleotopography of Bouley et al. (2016) and distinguished by total initial water inventory and obliquity. The black line indicates the freezing point of water. See Table 1 for descriptions of each simulation.

et al., 2016). By eye it can be seen from Figure 13 that the western portion of this band is higher (and hence colder) terrain while the center and eastern band is lower (and hence warmer) terrain. Figures 14 and 15 display annual total precipitation and annual total liquid precipitation for six simulations using the paleotopography and can be directly compared with Figures 10 and 11, which use modern topography. However, note that the scales of those two sets of figures are different to better highlight areas of higher precipitation in the paleotopography simulations.

Simply, there is far more precipitation in simulations with paleotopography. Each simulation with paleotopography has higher maximum precipitation than the comparable simulation with modern topography. However, as can be seen by comparing Figures 14 and 15, those maxima occur as snowfall over the high

Paleo Topography Annual Total Precipitation

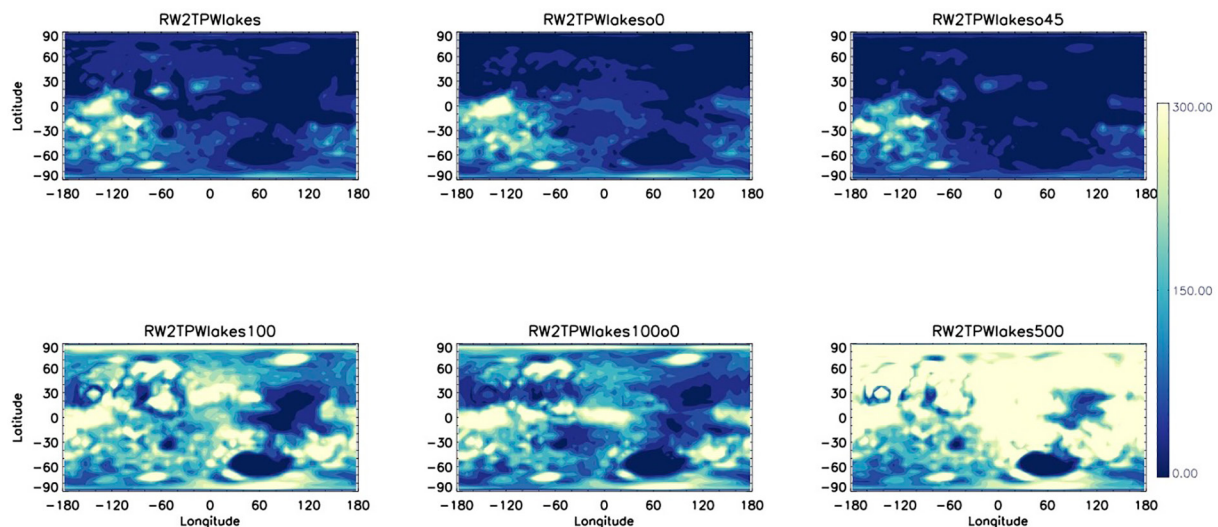


**Figure 14.** Annual total precipitation (mm) for 6 ROCKE-3D simulations distinguished by total initial water inventory and obliquity and using martian paleotopography. All water is initialized in lakes and then moved through the climate system. Note the different scale relative to Figure 10. See Table 1 for descriptions of each simulation.



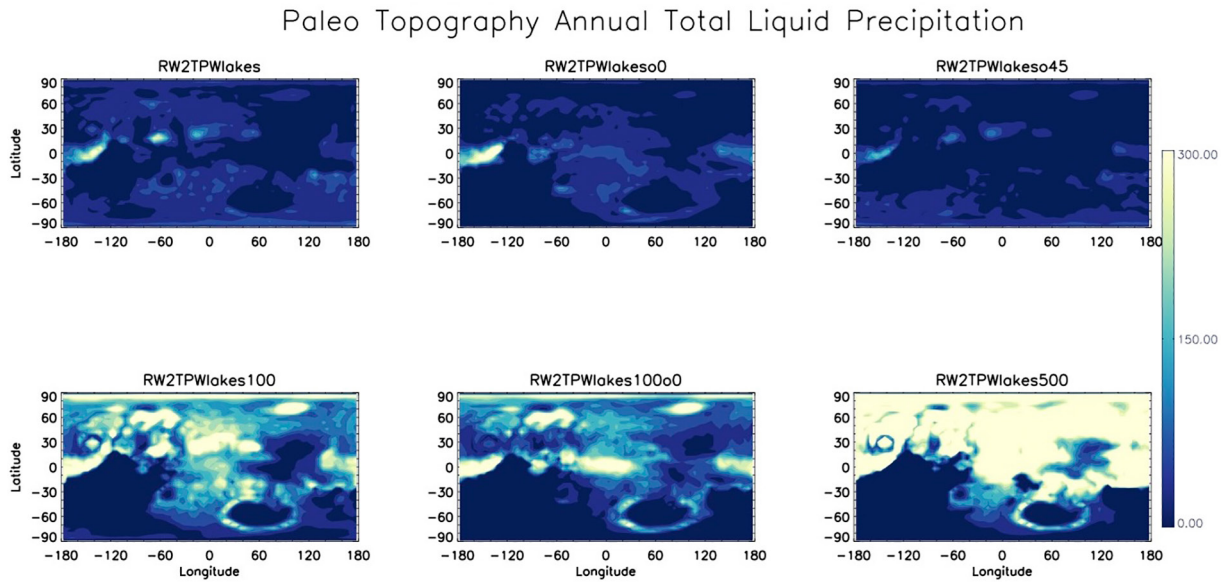


**Figure 15.** Same as Figure 14 except for annual total liquid precipitation (mm).

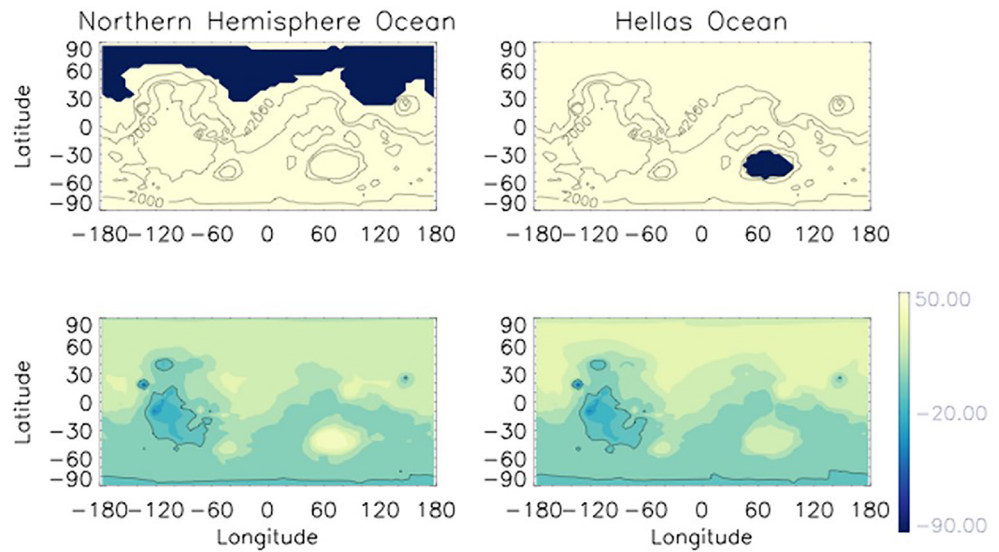
terrain in the southwest hemisphere of the planet. Unlike the simulations with modern topography, precipitation increases with increasing global water inventory. Simulations with 100 m or 500 m GEL water inventories see far more precipitation in the northern hemisphere due to the more abundant surface liquid water (in the form of lakes) in the northern hemisphere lowlands in those simulations.

Figure 15 shows that the planet is strongly divided between locations with predominant snowfall and those with predominant rainfall in the paleotopography simulations. Comparing Figure 15 to Figure 13 shows that areas with annual mean temperatures below freezing see very little or no rainfall. Much of the rainfall occurs in the northern hemisphere in all the simulations, but there is rainfall in the southern hemisphere low latitudes, particularly from 60°W to 180°E. This partially overlaps the expected region of the valley network formations if they formed prior to Tharsis and associated true polar wander (Bouley et al., 2016), but the western portion of this region does not have any significant rainfall in any of our simulations. Using the paleotopography, the simulations with either 0° or modern (25.19°) obliquity produce rainfall in this latitude band, with slightly more rainfall in the simulations with modern obliquity. Again, 45° obliquity is not consistent with rainfall over locations with valley network formations.

### 3.3. Ocean Simulations

Our final set of simulations uses ROCKE-3D's fully coupled dynamic ocean capability. Most other published ancient Mars ocean simulations used mixed layer oceans (e.g., Kamada et al., 2020). All previously discussed simulations with surface liquid water use dynamic lakes that form or evaporate based on precipitation patterns. In these simulations, water is initialized in oceans. We began a wide spectrum of such simulations, but the majority did not reach radiative and hydrological equilibrium before a shallow point of the ocean froze across the full depth. This freezing crashes the model and ends the simulation. Two ocean simulations did reach equilibrium, using modern topography and obliquity values. Following a long history of research discussing the possibility of an ancient martian northern hemisphere ocean (e.g., Di Achille & Hynek, 2010), we simulate such a northern ocean. Additionally, since Hellas basin is the lowest topographic point on the planet, we conduct a simulation with a Hellas ocean. Here, we introduce the impacts of these oceans on the broader planetary climate and reserve more in-depth analysis (hopefully with additional successful simulations) to future work.

Figure 16 provides an initial orientation to our two simulations with fully coupled dynamic oceans. The northern hemisphere ocean fills the northern lowlands Arcadia, Acidalia, and Utopia Planitiae to the –3,900 m isohypse, whereas the Hellas ocean fills much of that basin to the same level. Hence, the northern



**Figure 16.** The location of the northern hemisphere ocean and Hellas ocean (dark fill) and planetary topography (lines contoured at  $-2,000$ ,  $0$ , and  $2,000$  m; top row). The annual average surface temperatures for those two simulations ( $^{\circ}\text{C}$ ; bottom row).

ocean has a maximum depth of  $\sim 1,200$  m (corresponding to northern Acidalia Planitia) and the Hellas ocean has a maximum depth of  $\sim 3,000$  m. The bottom two panels of Figure 16 should look quite similar to those of the bottom middle two panels of Figure 5 since they use the same atmospheric gas composition. The subtle differences relate to the moderating influence of the oceans. The ocean basins are cooler than equivalent land surfaces in comparable simulations.

Our goal for the ocean simulations is to see if the ability of oceans to alter planetary climates through ocean heat transport, their greater thermal inertia, and effect on atmospheric flows and precipitation patterns could be manifested in a way that would make a temperate Noachian climate on Mars more durable. In other words, would the creation of a Noachian ocean on Mars help stabilize and warm the climate in a way that would help perpetuate that temperature climate for a longer duration than might otherwise be true? To diagnose this, we compare our two ocean simulations with the RW2lakes simulation. The ocean simulations have identical atmospheric pressure and gas compositions to the RW2lakes simulation as well as using modern topography and obliquity. As noted earlier, when using modern topography, the initial water inventory of the planet did not alter the final stable end climactic state, so no significant difference would be found in comparing the ocean simulations to the RW2lakes500 (with 500 m GEL water), for example.

Figure 17 demonstrates how the two ocean configurations alter the simulated climate. As seen in the top row, there is very little difference ( $<1^{\circ}\text{C}$ ) in annual average surface temperature for most of the planet if an ocean is present. Only the ocean itself, which is notably cooler than open dry ground, produces a change to annual average temperatures. This, alone, answers one of our questions regarding the influence of an ancient ocean on Noachian martian climate. Both a northern hemisphere or Hellas ocean are inefficiently distributed to allow substantial meridional heat transport which could help warm the planet and redistribute energy through the climate system. Hence, there is a marginal effect on planetary surface temperature. Note, however, that a 2-bar martian atmosphere does have very efficient *atmospheric* meridional heat transport due to the greater mass per unit area relative to Earth. The effect of atmospheric density on heat transport is discussed in the context of tidally locked planets around M-stars by, for example, Joshi et al. (1997) and Wordsworth (2015).

There is, however, a notable change in precipitation patterns around the planet. This is expected due to the larger surface liquid water inventory allowing increased evaporation and more available liquid water in the climate system. Recall that one key finding of the simulations with surface liquid water initialized in active lakes is that water is cold-trapped on Tharsis. The ocean simulations do produce widespread snow and ice cover on Tharsis, as did those with active lakes, but the simulation cannot evaporate the ocean and redeposit

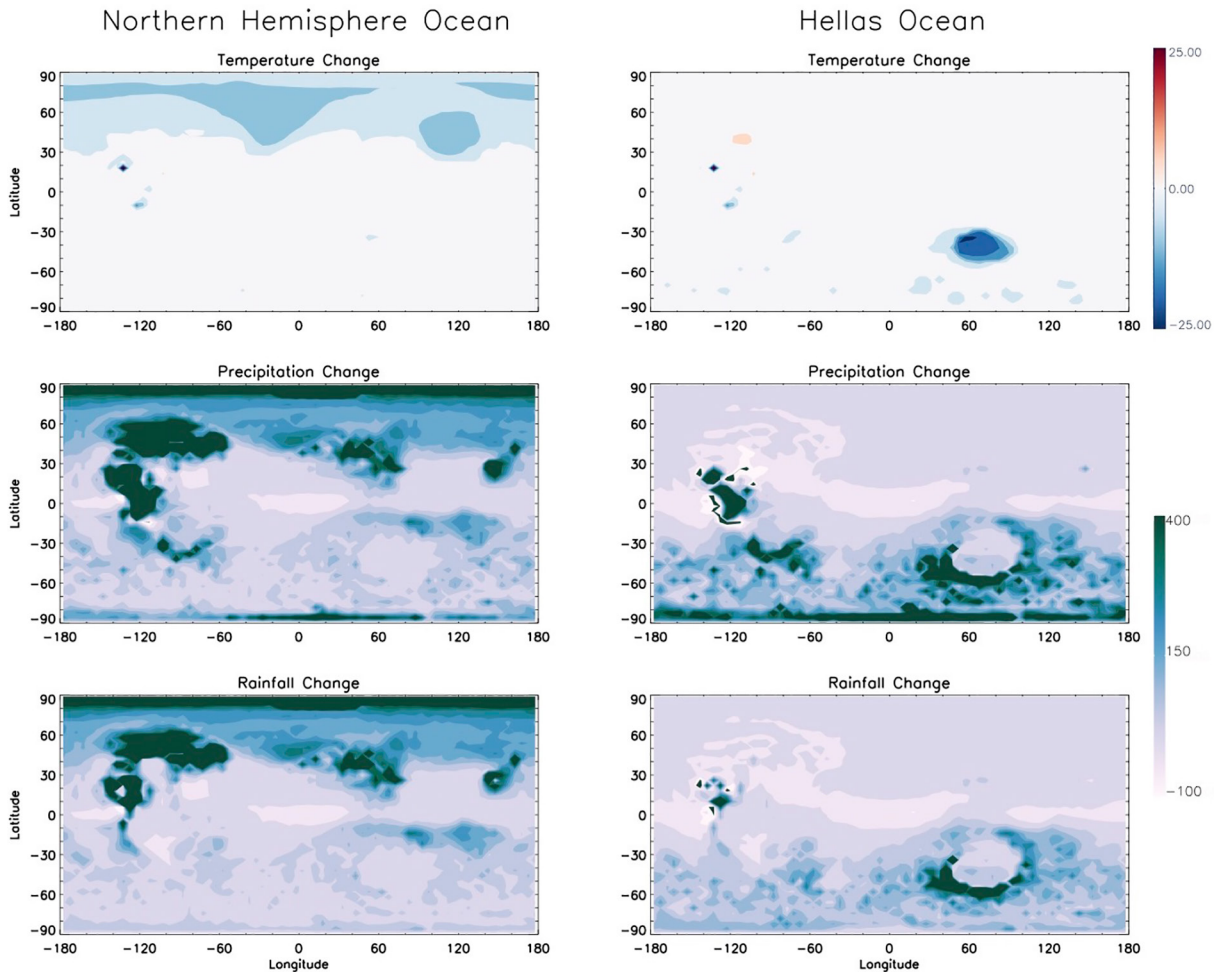


**Figure 17.** Change in annual average surface temperature ( $^{\circ}\text{C}$ , top row), change in annual precipitation (mm, middle row), and change in annual rainfall (mm, bottom row) when comparing the RW2lakes simulation to the northern hemisphere ocean simulation (left column) and Hellas ocean simulation (right column).

it as snow on Tharsis as may happen over geologic time in such a situation. These ocean simulations are hydrologically equilibrated, but it is reasonable to assume that ocean depth would drop slowly through time as water is deposited at the south pole and Tharsis. Indeed, as shown in Figure 17, precipitation near Tharsis is increased in these simulations, particularly for the northern hemisphere ocean simulation (to be expected given the proximity of the ocean to the Tharsis highlands). The Hellas ocean sees increased precipitation throughout the southern hemisphere, while the greatest change for the northern hemisphere ocean simulation is over that ocean itself.

Most notably, rainfall increases throughout the southern hemisphere and along the dichotomy boundary, including over many locations with valley network formations, with the Hellas ocean simulation. In the northern hemisphere ocean simulation, there is also a modest increase of rainfall along the dichotomy boundary (particularly from 60-150 $^{\circ}\text{E}$ ). There is also much more rainfall near Elysium Mons (25 $^{\circ}\text{N}$ , 140 $^{\circ}\text{W}$ ).

#### 4. Conclusions

In this work we seek to test whether the climate on Noachian Mars could have maintained “warm and wet” conditions with reasonable constraints on surface air pressure (2 bar or less) and the possible availability of  $\text{H}_2\text{-CO}_2$  CIA using ROCKE-3D, a capable and flexible GCM. With ROCKE-3D, the answer to this question is “yes.”  $\text{CO}_2$ -dominated atmospheres with surface pressures above  $\sim 1.5$  bar and  $\text{H}_2$  mixing ratios of  $\geq 3\%$

produce global mean surface temperatures above the freezing point of water. Our work is agnostic to the source of the H<sub>2</sub> and its duration in the atmosphere.

Note, however, that in these initial simulations without significant amounts of water (indeed, with a global water inventory more akin to modern Mars), the warmest locations are in the northern hemisphere lowlands and Hellas basins. These are both locations far removed from the places with geologic evidence of past fluvial activity in the southern hemisphere highlands near the topographic dichotomy boundary and elsewhere. Much of the southern hemisphere and Tharsis region have annual average temperatures well below freezing.

Additionally, some of our tested atmospheric gas mixtures include CH<sub>4</sub>. We find that a small amount of CH<sub>4</sub>, 1% in our simulations, could have had important implications for ancient water loss on Mars. Simulations that include CH<sub>4</sub> produce a weak and leaky stratosphere, where warming temperatures limit water cloud formation, but where the upper tropospheric cold trap is insufficient to limit vertical transport of water into the stratosphere where it could be photodissociated and lost to space. Simulations without CH<sub>4</sub> have thicker water clouds in the upper troposphere, which acts as a more efficient hygropause, reducing water flux into the upper atmosphere. Future work should address the implications of CH<sub>4</sub> and water ice clouds on water loss from Noachian Mars in more detail.

After finding an atmospheric gas mixture that produced global mean temperatures above freezing (RW2 = 94% CO<sub>2</sub>, 5% H<sub>2</sub>, and 1% CH<sub>4</sub> following Wordsworth et al., 2017), our second set of simulations has looked at the hydrological cycle of the planet under these possible warm and wet conditions. Using modern topography, the vast majority of water on the planet, regardless of the initial water inventory, is cold-trapped on the high and frigid Tharsis plateau. ROCKE-3D does not have a land ice or glacier parameterization that could simulate the eventual flow of these glaciers and determine how glacial melt could recharge the system. But, regardless, the planet is left with comparatively little water actively cycling. We find planetary obliquity is key to determining where precipitation falls as rain or snow in these simulations. Simulations with 0° obliquity produce greater rainfall near locations with valley network formations. Simulations with 45° obliquity are slightly cooler than those with either modern or 0° obliquity and have rainfall patterns that are inconsistent with the geologic evidence for fluvial activity on Noachian Mars. Note our simulations do not include the physics of CO<sub>2</sub> condensation. But, importantly, many of our simulations that included H<sub>2</sub> had surface temperatures remain above the CO<sub>2</sub> condensation temperature, regardless of obliquity.

The timing of the formation of Tharsis relative to the valley network formations is critical to understanding the climatic conditions under which they formed. Simulations using a plausible paleotopography (see Bouley et al. (2016)) have increased amounts of precipitation globally due to the lack of Tharsis acting as a cold trap for snow and ice. Again, simulations with modern or 0° obliquity are more consistent with rainfall over locations with valley network formations than 45° obliquity.

If Noachian Mars had oceans (following Tharsis emplacement with modern topography), the most plausible locations for those oceans in the northern hemisphere lowlands and Hellas basin are inefficient for meridional heat transport. The global climate is no warmer when an ocean is present than when it is absent, assuming the background atmospheric composition is supportive of surface liquid water already. The presence of oceans does alter precipitation patterns, however, and precipitation and rainfall are increased over much of the planet. A Hellas ocean in particular produces increased rainfall in many locations where valley network formations and paleolakes are seen in the modern surface geology.

## Data Availability Statement

Model input and boundary condition files, rundecks (simulation setup files), and final output files are available here: doi: <https://doi.org/10.5281/zenodo.4926123> (Guzewich et al., 2021).

## References

- Abramopoulos, F., Rosenzweig, C., & Choudhury, B. (1988). Improved ground hydrology calculations for global climate models (GCMs): Soil water movement and evapotranspiration. *Journal of Climate*, 1(9), 921–941. [https://doi.org/10.1175/1520-0442\(1988\)001<0921:IGHCFG>2.0.CO;2](https://doi.org/10.1175/1520-0442(1988)001<0921:IGHCFG>2.0.CO;2)

## Acknowledgments

Guzewich, Way, Del Genio, Aleinov, Wolf, and Tsigaridis were supported by the NASA Nexus for Exoplanet System Science program that helped develop the ROCKE-3D GCM. Guzewich, Way, Aleinov, Wolf, and Tsigaridis acknowledge support from the GSFC Sellers Exoplanet Environments Collaboration (SEEC), which is funded by the NASA Planetary Science Division's Internal Scientist Funding Model. Resources supporting this work were provided by the NASA High-End Computing (HEC) Program through the NASA Center for Climate Simulation (NCCS) at Goddard Space Flight Center. The authors thank Bouley et al. (2016) for helpfully including the paleotopographic file in their supplemental material to make some of these simulations plausible. The authors thank Michael Mischna and an anonymous reviewer for their helpful comments that improved this manuscript.

- Aleinov, I., Way, M., Harman, C. E., Tsigaridis, K., Wolf, E. T., & Gronoff, G. (2019). Modeling a transient secondary paleolunar atmosphere: 3-D simulations and analysis. *Geophysical Research Letters*, *46*, 5107–5116. <https://doi.org/10.1029/2019GL082494>
- Amundsen, D. S., Mayne, N. J., Baraffe, I., Manners, J., Tremblin, P., Drummond, B., et al. (2016). The UK Met Office global circulation model with a sophisticated radiation scheme applied to the hot Jupiter HD 209458b. *Astronomy & Astrophysics*, *595*, A36. <https://doi.org/10.1051/0004-6361/201629183>
- Batalha, N., Domagal-Goldman, S. D., Ramirez, R., & Kasting, J. F. (2015). Testing the early Mars H<sub>2</sub>-CO<sub>2</sub> greenhouse hypothesis with a 1-D photochemical model. *Icarus*, *258*, 337–349. <https://doi.org/10.1016/j.icarus.2015.06.016>
- Bouley, S., Baratoux, D., Matsuyama, I., Forget, F., Séjourné, A., Turbet, M., & Costard, F. (2016). Late Tharsis formation and implications for early Mars. *Nature*, *531*, 344–347. <https://doi.org/10.1038/nature17171>
- Brown, L. R., Sung, K., Benner, D. C., Devi, V. M., Boudon, V., Gabard, T., et al. (2013). Methane line parameters in the HITRAN2012 database. *Journal of Quantitative Spectroscopy and Radiative Transfer*, *130*, 201–219. <https://doi.org/10.1016/j.jqsrt.2013.06.020>
- Bryne, B., & Goldblatt, C. (2015). Diminished greenhouse warming from Archean methane due to solar absorption lines. *Climate of the Past*, *11*, 559–570. <https://doi.org/10.5194/cp-11-559-2015>
- Carr, M. H. (1996). *Water on Mars* (pp. 229). New York: Oxford University Press. <https://doi.org/10.1016/b978-075069707-1/50056-0>
- Carter, J., Poulet, F., Bibring, J.-P., Mangold, N., & Murchie, S. (2013). Hydrated minerals on Mars as seen by the CRISM and OMEGA imaging spectrometers: Updated global view. *Journal of Geophysical Research: Planets*, *118*, 831–858. <https://doi.org/10.1029/2012JE004145>
- Cassanelli, J. P., & Head, J. W., III (2015). Firn densification in a Late Noachian “icy highlands” Mars: Implications for ice sheet evolution and thermal response. *Icarus*, *253*, 243–255. <https://doi.org/10.1016/j.icarus.2015.03.004>
- Cassata, W., Schuster, D. L., Renne, P. R., & Weiss, B. P. (2012). Trapped Ar isotopes in meteorite ALH 84001 indicate Mars did not have a thick ancient atmosphere. *Icarus*, *221*, 461–465. <https://doi.org/10.1016/j.icarus.2012.05.005>
- Citron, R. I., Manga, M., & Hemingway, D. J. (2018). Timing of oceans on Mars from shoreline deformation. *Nature*, *555*(7698), 643–646. <https://doi.org/10.1038/nature26144>
- Claire, M. W., Sheets, J., Cohen, M., Ribas, I., Meadows, V. S., & Catling, D. (2012). The evolution of solar flux from 0.1 nm to 160 μm: Quantitative estimates for planetary studies. *The Astrophysical Journal*, *757*(12), 95. <https://doi.org/10.1088/0004-637x/757/1/95>
- Clancy, R., Grossman, A. W., Wolff, M. J., James, P. B., Rudy, D. J., Billawala, Y. N., et al. (1996). Water vapor saturation at low altitudes around Mars aphelion: A key to Mars climate. *Icarus*, *122*, 36–62. <https://doi.org/10.1006/icar.1996.0108>
- Clough, S. A., Shephard, M. W., Mlawer, E. J., Delamre, J. S., Iacono, M. J., Cady-Pereira, K., et al. (2005). Atmospheric radiative transfer modeling: A summary of the AER codes. *Journal of Quantitative Spectroscopy and Radiative Transfer*, *91*, 233–244. <https://doi.org/10.1016/j.jqsrt.2004.05.058>
- Del Genio, A. D., Way, M. J., Amundsen, D. S., Aleinov, I., Kelley, M., Kiang, N. Y., & Clune, T. L. (2019). Habitable climate scenarios for Proxima Centauri b with a dynamic ocean. *Astrobiology*, *19*(1), 99–125. <https://doi.org/10.1089/ast.2017.1760>
- Del Genio, A. D., Wu, J., Wolf, A. B., Chen, Y., Yao, M.-S., & Kim, D. (2015). Constraints on cumulus parameterization from simulations of observed MJO events. *Journal of Climate*, *28*(16), 6419–6442. <https://doi.org/10.1175/JCLI-D-14-00832.1>
- Di Achille, G., & Hynek, B. M. (2010). Ancient Ocean on Mars supported by global distribution of deltas and valleys. *Nature Geoscience*, *3*, 459–463. <https://doi.org/10.1038/ngeo891>
- Edwards, J. M. (1996). Efficient calculation of infrared fluxes and cooling rates using the two-stream equations. *Journal of the Atmospheric Sciences*, *53*, 1921–1932. [https://doi.org/10.1175/1520-0469\(1996\)053<1921:ecoifa>2.0.co;2](https://doi.org/10.1175/1520-0469(1996)053<1921:ecoifa>2.0.co;2)
- Edwards, J. M., Havemann, S., Thelen, J.-C., & Baran, A. J. (2007). A new parameterization for the radiative properties of ice crystals: Comparison with existing schemes and impact in a GCM. *Atmospheric Research*, *83*(1), 19–35. <https://doi.org/10.1016/j.atmosres.2006.03.002>
- Edwards, J. M., & Slingo, A. (1996). Studies with a flexible new radiation code. I: Choosing a configuration for a large-scale model. *Quarterly Journal of the Royal Meteorological Society*, *122*(531), 689–719. <https://doi.org/10.1002/qj.49712253107>
- Ehlmann, B., Mustard, J., Murchie, S., Bibring, J.-P., Meunier, A., Fraeman, A. A., & Langevin, Y. (2011). Subsurface water and clay mineral formation during the early history of Mars. *Nature*, *479*, 53–60. <https://doi.org/10.1038/nature10582>
- Fassett, C. I., & Head, J. W. (2005). Fluvial sedimentary deposits on Mars: Ancient deltas in a crater lake in the Nili Fossae region. *Geophysical Research Letters*, *32*, L14201. <https://doi.org/10.1029/2005GL023456>
- Fastook, J. L., & Head, J. W., III (2015). Glaciation in the Late Noachian icy highlands: Ice accumulation, distribution, flow rates, basal melting, and top-down melting rates and patterns. *Planetary and Space Science*, *106*, 82–98. <https://doi.org/10.1016/j.pss.2014.11.028>
- Fastook, J. L., Head, J. W., III, Marchant, D. R., Forget, F., & Madeleine, J. B. (2012). Early Mars climate near the Noachian-Hesperian boundary: Independent evidence for cold conditions from basal melting of the south polar ice sheet (Dorsa Argentea formation) and implications for valley network formation. *Icarus*, *219*, 25–40. <https://doi.org/10.1016/j.icarus.2012.02.013>
- Forget, F., & Pierrehumbert, R. (1997). Warming early Mars with carbon dioxide clouds that scatter infrared radiation. *Science*, *278*(5341), 1273–1276. <https://doi.org/10.1126/science.278.5341.1273>
- Forget, F., Wordsworth, R., Millour, E., Madeleine, J.-B., Kerber, L., Leconte, J., et al. (2013). 3D modelling of the early Martian climate under a denser CO<sub>2</sub> atmosphere: Temperatures and CO<sub>2</sub> ice clouds. *Icarus*, *222*(1), 81–99. <https://doi.org/10.1016/j.icarus.2012.10.019>
- Godin, P. J., Ramirez, R. M., Campbell, C. L., Wizenberg, T., Nguyen, T. G., Strong, K., & Moores, J. E. (2020). Collision-induced absorption of CH<sub>4</sub>-CO<sub>2</sub> and H<sub>2</sub>-CO<sub>2</sub> complexes and their effect on the ancient Martian atmosphere. *Journal of Geophysical Research: Planets*, *125*(12), e2019JE006357. <https://doi.org/10.1029/2019JE006357>
- Gough, D. O. (1981). Solar interior structure and luminosity variations. *Solar Physics*, *74*, 21–34. [https://doi.org/10.1007/978-94-010-9633-1\\_4](https://doi.org/10.1007/978-94-010-9633-1_4)
- Grant, J. A., Wilson, S. A., Mangold, N., Calef, F., & Grotzinger, J. P. (2014). The timing of alluvial activity in Gale crater, Mars. *Geophysical Research Letters*, *41*, 1142–1149. <https://doi.org/10.1002/2013GL058909>
- Grotzinger, J. P., Sumner, D. Y., Kah, L. C., Stack, K., Gupta, S., Edgar, L., et al. (2014). A habitable Fluvio-Lacustrine environment at Yellowknife Bay, Gale Crater, Mars. *Science*, *343*, 6169. <https://doi.org/10.1126/science.1242777>
- Guzewich, S., Way, M., Aleinov, I., Wolf, E., Del Genio, A., Wordsworth, R., & Tsigaridis, K. (2021). 3D simulations of the early Martian hydrological cycle mediated by a H<sub>2</sub>-CO<sub>2</sub> greenhouse. <https://doi.org/10.5281/zenodo.4926123>
- Haberle, R. M., Zahnle, K., Barlow, N. G., & Steakley, K. E. (2019). Impact degassing of H<sub>2</sub> on early Mars and its effect on the climate system. *Geophysical Research Letters*, *46*, 13355–13362. <https://doi.org/10.1029/2019GL084733>
- Hansen, J., Russell, G., Rind, D., Stone, P., Lacis, A., Lebedeff, S., et al. (1983). Efficient three-dimensional global models for climate studies: Models I and II. *Monthly Weather Review*, *111*(2), 609–662. [https://doi.org/10.1175/1520-0493\(1983\)111<0609:etdgmf>2.0.co;2](https://doi.org/10.1175/1520-0493(1983)111<0609:etdgmf>2.0.co;2)
- Hayworth, B. P. C., Koppapur, R. K., Haqq-Misra, J., Batalha, N. E., Payne, R. C., Foley, B. J., et al. (2020). Warming early Mars with climate cycling: The effect of CO<sub>2</sub>-H<sub>2</sub> collision-induced absorption. *Icarus*, *345*, 113770. <https://doi.org/10.1016/j.icarus.2020.113770>
- Hirschmann, M. M., & Withers, A. C. (2008). Ventilation of CO<sub>2</sub> from a reduced mantle and consequences for the early Martian greenhouse. *Earth and Planetary Science Letters*, *270*, 147–155. <https://doi.org/10.1016/j.epsl.2008.03.034>

- Hurowitz, J. A., Fischer, W. W., Tosca, N. J., & Milliken, R. E. (2010). Origin of acidic surface waters and the evolution of atmospheric chemistry on early Mars. *Nature Geoscience*, 3(5), 323–326. <https://doi.org/10.1038/ngeo831>
- Hynek, B. M., Beach, M., & Hoke, M. R. T. (2010). Updated global map of Martian valley networks and implications for climate and hydrologic processes. *Journal of Geophysical Research*, 115, E09008. <https://doi.org/10.1029/2009JE003548>
- Hynek, B. M., & Phillips, R. J. (2001). Evidence for extensive denudation of the Martian Highlands. *Geology*, 21(5), 407–410. [https://doi.org/10.1130/0091-7613\(2001\)029<0407:efedot>2.0.co;2](https://doi.org/10.1130/0091-7613(2001)029<0407:efedot>2.0.co;2)
- Irwin, R. P., Howard, A. D., Craddock, R. A., & Moore, J. M. (2005). An intense terminal epoch of widespread fluvial activity on early Mars: 2. Increased runoff and paleolake development. *Journal of Geophysical Research*, 110, E12S15. <https://doi.org/10.1029/2005JE002460>
- Jakosky, B. M., Brain, D., Chaffin, M., Curry, S., Deighan, J., Grebowsky, J., et al. (2018). Loss of the Martian atmosphere to space: Present-day loss rates determined from MAVEN observations and integrated loss through time. *Icarus*, 315, 146–157. <https://doi.org/10.1016/j.icarus.2018.05.030>
- Joshi, M. M., Haberle, R. M., & Reynolds, R. T. (1997). Simulations of the atmospheres of synchronously rotating terrestrial planets orbiting M dwarfs: Conditions for atmospheric collapse and implications for habitability. *Icarus*, 129, 450–465. <https://doi.org/10.1006/icar.1997.5793>
- Kamada, A., Kuroda, T., Kasaba, Y., Terada, N., Nakagawa, H., & Toriumi, K. (2020). A coupled atmosphere-hydrosphere climate model of early Mars: A “cool and wet” scenario for the formation of water channels. *Icarus*, 338, 113567. <https://doi.org/10.1016/j.icarus.2019.113567>
- Kasting, J. F. (1991). CO<sub>2</sub> condensation and the climate of early Mars. *Icarus*, 94(1), 1–13. [https://doi.org/10.1016/0019-1035\(91\)90137-1](https://doi.org/10.1016/0019-1035(91)90137-1)
- Kasting, J. F. (1997). Warming early Earth and Mars. *Science*, 279, 5316–1215. <https://doi.org/10.1126/science.276.5316.1213>
- Kerber, L., Forget, F., & Wordsworth, R. D. (2015). Sulfur in the early Martian atmosphere revisited: Experiments with a 3-D global climate model. *Icarus*, 261, 133–148. <https://doi.org/10.1016/j.icarus.2015.08.011>
- Kite, E. S., Sneed, J., Mayer, D. P., & Wilson, S. A. (2017). Persistent or repeated surface habitability on Mars during the late Hesperian—Amazonian. *Geophysical Research Letters*, 44, 3991–3999. <https://doi.org/10.1002/2017GL072660>
- Kite, E. S., Williams, J.-P., Lucas, A., & Aharonson, O. (2014). Low palaeopressure of the Martian atmosphere estimated from the size distribution of ancient craters. *Nature Geoscience*, 7, 335–339. <https://doi.org/10.1038/ngeo2137>
- Kopparapu, R. K., Ramirez, R., Kasting, J. F., Eymet, V., Robinson, T. D., Mahadevan, S., et al. (2013). Habitable zones around main-sequence stars: New estimates. *The Astrophysical Journal*, 765(16), 131. <https://doi.org/10.1088/0004-637x/765/2/131>
- Kuhn, W. R., & Atreya, S. K. (1979). Ammonia photolysis and the greenhouse effect in the primordial atmosphere of the Earth. *Icarus*, 37, 207–213. [https://doi.org/10.1016/0019-1035\(79\)90126-X](https://doi.org/10.1016/0019-1035(79)90126-X)
- Lean, J., Beer, J., & Bradley, S. (1995). Reconstruction of solar irradiance since 1610: Implications for climate change. *Geophysical Research Letters*, 22, 3195–3198. <https://doi.org/10.1029/95gl03093>
- Malin, M. C., & Edgett, K. S. (2000). Sedimentary rocks of early Mars. *Science*, 290(5498), 1927–1937. <https://doi.org/10.1126/science.290.5498.1927>
- Manga, M., Patel, A., Dufek, J., & Kite, E. S. (2012). Wet surface and dense atmosphere on early Mars suggested by the bomb sag at Home Plate, Mars. *Geophysical Research Letters*, 39, L01202. <https://doi.org/10.1029/2011GL050192>
- Masursky, H. (1973). An overview of geological results from Mariner 9. *Journal of Geophysical Research*, 78(20), 4009–4030. <https://doi.org/10.1029/JB078i020p04009>
- Matsuyama, I., & Manga, M. (2010). Mars without the equilibrium rotational figure, Tharsis, and the remnant rotational figure. *Journal of Geophysical Research*, 115, E12020. <https://doi.org/10.1029/2010je003686>
- Mischna, M. A., Baker, V., Milliken, R., Richardson, M., & Lee, C. (2013). Effects of obliquity and water vapor/trace gas greenhouses in the early Martian climate. *Journal of Geophysical Research: Planets*, 118, 560–576. <https://doi.org/10.1002/jgre.20054>
- Mondelain, D., Boulet, C., & Hartmann, J.-M. (2021). The binary absorption coefficients for H<sub>2</sub> + CO<sub>2</sub> mixtures in the 2.12–2.35 μm spectral region determined by CRDS and by semi-empirical calculations. *Journal of Quantitative Spectroscopy and Radiative Transfer*, 260, 107454. <https://doi.org/10.1016/j.jqsrt.2020.107454>
- Murchie, S., Roach, L., Seelos, F., Milliken, R., Mustard, J., Arvidson, R., et al. (2009). Evidence for the origin of layered deposits in Candor Chasma, Mars, from mineral composition and hydrologic modeling. *Journal of Geophysical Research*, 114, E00D05. <https://doi.org/10.1029/2009JE003343>
- Navarro, T., Madeleine, J.-B., Forget, F., Spiga, A., Millour, E., Montmessin, F., & Määttänen, A. (2014). Global climate modeling of the Martian water cycle with improved microphysics and radiatively active water ice clouds. *Journal of Geophysical Research: Planets*, 119, 1479–1495. <https://doi.org/10.1002/2013JE004550>
- Palumbo, A. M., & Head, J. W. (2018). Early Mars climate history: Characterizing a “warm and wet” Martian climate with a 3-D global climate model and testing geological predictions. *Geophysical Research Letters*, 45, 10249–10258. <https://doi.org/10.1029/2018GL079767>
- Palumbo, A. M., Head, J. W., & Wilson, L. (2020). Rainfall on Noachian Mars: Nature, timing, and influence on geologic processes and climate history. *Icarus*, 347, 113782. <https://doi.org/10.1016/j.icarus.2020.113782>
- Pieri, D. C. (1980). Martian valleys: Morphology, distribution, age, and origin. *Science*, 210(4472), 895–897. <https://doi.org/10.1126/science.210.4472.895>
- Pike, W. T., Stauffer, U., Hecht, M. H., Goetz, W., Parrat, D., Sykulka-Lawrence, H., et al. (2011). Quantification of the dry history of the Martian soil inferred from in situ microscopy. *Geophysical Research Letters*, 38, L24201. <https://doi.org/10.1029/2011GL049896>
- Pollack, J. B. (1979). Climate change on the terrestrial planets. *Icarus*, 37, 479–553. [https://doi.org/10.1016/0019-1035\(79\)90012-5](https://doi.org/10.1016/0019-1035(79)90012-5)
- Pollack, J. B., Kasting, J. F., Richardson, S. M., & Poliakov, K. (1987). The case for a wet, warm climate on early Mars. *Icarus*, 71, 203–224. [https://doi.org/10.1016/0019-1035\(87\)90147-3](https://doi.org/10.1016/0019-1035(87)90147-3)
- Postawko, S. E., & Kuhn, W. R. (1986). Effect of the greenhouse gases (CO<sub>2</sub>, H<sub>2</sub>O, SO<sub>2</sub>) on Martian paleoclimate. *Journal of Geophysical Research*, 91(B4), 431–438. <https://doi.org/10.1029/JB091iB04pD0431>
- Ramirez, R., Kopparapu, R., Zuger, M., Robinson, T. D., Freedman, R., & Kasting, J. F. (2014). Warming early Mars with CO<sub>2</sub> and H<sub>2</sub>. *Nature Geoscience*, 7, 59–63. <https://doi.org/10.1038/ngeo2000>
- Roe, H. G. (2012). Titan’s methane weather. *Annual Review of Earth and Planetary Sciences*, 40, 355–382. <https://doi.org/10.1146/annurev-earth-040809-152548>
- Rosenzweig, C., & Abramopoulos, F. (1997). Land-surface model development for the GISS GCM. *Journal of Climate*, 10(8), 2040–2054. [https://doi.org/10.1175/1520-0442\(1997\)010<2040:LSMDFT>2.0.CO;2](https://doi.org/10.1175/1520-0442(1997)010<2040:LSMDFT>2.0.CO;2)
- Rothman, L. S., Gordon, I. E., Babikov, Y., Barbe, A., Benner, D. C., Bernath, P. F., et al. (2013). The HITRAN2012 molecular spectroscopic database. *Journal of Quantitative Spectroscopy and Radiative Transfer*, 130, 4–50. <https://doi.org/10.1016/j.jqsrt.2013.07.002>

- Schmidt, G. A., Ruedy, R., Hansen, J. E., Aleinov, I., Bell, N., Bauer, M., et al. (2006). Present-day atmospheric simulations using GISS ModelE: Comparison to in situ, satellite, and reanalysis data. *Journal of Climate*, *19*(2), 153–192. <https://doi.org/10.1175/jcli3612.1>
- Schon, S. C., Head, J. W., & Fassett, C. I. (2012). An overfilled lacustrine system and progradational delta in Jezero crater, Mars: Implications for Noachian climate. *Planetary and Space Science*, *67*, 28–45. <https://doi.org/10.1016/j.pss.2012.02.003>
- Tarnas, J. D., Mustard, J. F., Lollar, B. S., Bramble, M. S., Cannon, K. M., Palumbo, A. M., & Plesa, A. C. (2018). Radiolytic H<sub>2</sub> production on Noachian Mars: Implications for habitability and atmospheric warming. *Earth and Planetary Science Letters*, *502*, 133–145. <https://doi.org/10.1016/j.epsl.2018.09.001>
- Tian, F., Claire, M. W., Haqq-Misra, J. D., Smith, M., Crisp, D. C., Catling, D., et al. (2010). Photochemical and climate consequences of sulfur outgassing on early Mars. *Earth and Planetary Science Letters*, *295*, 412–418. <https://doi.org/10.1016/j.epsl.2010.04.016>
- Tosca, N. J., Ahmed, I. A., Tutolo, B. M., Ashpittel, A., & Hurowitz, J. A. (2018). Magnetite authigenesis and the warming of early Mars. *Nature Geoscience*, *11*(9), 635–639. <https://doi.org/10.1038/s41561-018-0203-8>
- Turbet, M., Boulet, C., & Karman, T. (2020). Measurements and semi-empirical calculations of CO<sub>2</sub> + CH<sub>4</sub> and CO<sub>2</sub> + H<sub>2</sub> collision-induced absorption across a wide range of wavelengths and temperatures. Application for the prediction of early Mars surface temperature. *Icarus*, *346*, 113762. <https://doi.org/10.1016/j.icarus.2020.113762>
- Turbet, M., & Forget, F. (2019). The paradoxes of the Late Hesperian Mars ocean. *Scientific Reports*, *9*, 5717. <https://doi.org/10.1038/s41598-019-42030-2>
- Turbet, M., Gillmann, C., Forget, F., Baudin, B., Palumbo, A., Head, J., & Karatekin, O. (2020). The environmental effects of very larger bolide impacts on early Mars explored with a hierarchy of numerical models. *Icarus*, *335*, 113419. <https://doi.org/10.1016/j.icarus.2019.113419>
- Urata, R. A., & Toon, O. B. (2013). Simulations of the Martian hydrologic cycle with a general circulation model: Implications for the ancient Martian climate. *Icarus*, *226*, 229–250. <https://doi.org/10.1016/j.icarus.2013.05.014>
- Warren, A. O., Kite, E. S., Williams, J. -P., & Horgan, B. (2019). Through the thick and thin: New constraints on Mars paleopressure history 3.8–4 Ga from small exhumed craters. *Journal of Geophysical Research: Planets*, *124*, 2793–2818. <https://doi.org/10.1029/2019JE006178>
- Way, M. J., Aleinov, I., Amundsen, D. S., Chandler, M. A., Clune, T., Del Genio, A. D., et al. (2017). Resolving orbital and climate keys of Earth and extraterrestrial environments with Dynamics 1.0: A general circulation model for simulating the climates of rocky planets. *The Astrophysical Journal - Supplement Series*, *231*(1), 12. <https://doi.org/10.3847/1538-4365/aa7a06>
- Way, M. J., & Del Genio, A. D. (2020). Venusian habitable climate scenarios: Modeling Venus through time and applications to slowly rotating Venus-like exoplanets. *Journal of Geophysical Research: Planets*, *125*, e2019JE006276. <https://doi.org/10.1029/2019JE006276>
- Way, M. J., Del Genio, A. D., Aleinov, I., Clune, T. L., Kelley, M., & Kiang, N. Y. (2018). Climates of warm Earth-like planets I 3D model simulations. *The Astrophysical Journal - Supplement Series*, *239*, 24. <https://doi.org/10.3847/1538-4365/aae9e1>
- Way, M. J., Del Genio, A. D., Kiang, N. Y., Sohl, L. E., Grinspoon, D. H., Aleinov, I., et al. (2016). Was Venus the first habitable world of our solar system? *Geophysical Research Letters*, *43*(16), 8376–8383. <https://doi.org/10.1002/2016GL069790>
- Williams, R. M. E., Grotzinger, J. P., Dietrich, W. E., Gupta, S., Sumner, D. Y., Wiens, R. C., et al. (2013). Martian fluvial conglomerates at Gale Crater. *Science*, *340*(1068), 6136–1072. <https://doi.org/10.1126/science.1237317>
- Wolf, E. T., & Toon, O. B. (2013). Hospitable Archean climates simulated by a general circulation model. *Astrobiology*, *13*, 656–673. <https://doi.org/10.1089/ast.2012.0936>
- Wordsworth, R. (2015). Atmospheric heat redistribution and collapse on tidally locked rocky planets. *The Astrophysical Journal*, *806*(2), 180. <https://doi.org/10.1088/0004-637x/806/2/180>
- Wordsworth, R., Forget, F., & Eymet, V. (2010). Infrared collision-induced and far-line absorption in dense CO<sub>2</sub> atmospheres. *Icarus*, *210*, 992–997. <https://doi.org/10.1016/j.icarus.2010.06.010>
- Wordsworth, R., Forget, F., Millour, E., Head, J. W., Madeleine, J. B., & Charnay, B. (2013). Global modelling of the early Martian climate under a denser CO<sub>2</sub> atmosphere: Water cycle and ice evolution. *Icarus*, *222*, 1–19. <https://doi.org/10.1016/j.icarus.2012.09.036>
- Wordsworth, R., & Pierrehumbert, R. (2013). Hydrogen-nitrogen greenhouse warming in Earth's early atmosphere. *Science*, *339*, 64–67. <https://doi.org/10.1126/science.1225759>
- Wordsworth, R. D. (2016). The climate of early Mars. *Annual Review of Earth and Planetary Sciences*, *44*, 381–408. <https://doi.org/10.1146/annurev-earth-060115-012355>
- Wordsworth, R. D., Kalugina, Y., Lokshtanov, S., Vigasin, A., Ehlmann, B., Head, J., et al. (2017). Transient reducing greenhouse warming on early Mars. *Geophysical Research Letters*, *44*, 665–671. <https://doi.org/10.1002/2016GL071766>
- Wordsworth, R. D., Kerber, L., Pierrehumbert, R. T., Forget, F., & Head, J. W. (2015). Comparison of “warm and wet” and “cold and icy” scenarios for early Mars in a 3-D climate model. *Journal of Geophysical Research: Planets*, *120*, 1201–1219. <https://doi.org/10.1002/2015JE004787>
- Yang, J., Leconte, J., Wolf, E. T., Goldblatt, C., Feldl, N., Merlis, T., et al. (2016). Differences in water vapor radiative transfer among 1D models can significantly affect the inner edge of the habitable zone. *The Astrophysical Journal*, *826*(11), 222. <https://doi.org/10.3847/0004-637x/826/2/222>